Mon. Not. R. Astron. Soc. **000**, 1–19 (2011) Printed 19 January 2013 (MN LaTeX style file v2.2)

arXiv:1104.2121v1 [astro-ph.CO] 12 Apr 2011

Properties of star-forming galaxies in a cluster and its surrounding structure at $z = 1.46$

Masao Hayashi,[1⋆] Tadayuki Kodama,[1,2] Yusei Koyama,[1,3]
Ken-ichi Tadaki,[1,3] Ichi Tanaka[2]
[1] *Optical and Infrared Astronomy Division, National Astronomical Observatory, Mitaka, Tokyo 181-8588, Japan*
[2] *Subaru Telescope, National Astronomical Observatory of Japan, 650 North A'ohoku Place, Hilo, HI 96720, USA*
[3] *Department of Astronomy, Graduate School of Science, University of Tokyo, Tokyo 113-0033, Japan*

Accepted 2011 April 8. Received 2011 April 8; in original form 2011 February 15

ABSTRACT

We conduct a wide-field narrow-band imaging survey of [O II] emitters in and around the XMMXCS J2215.9-1738 cluster at $z = 1.46$ with Subaru/Suprime-Cam. In a $32' \times 23'$ area, we select 380 [O II] emitting galaxies down to 1.4×10^{-17} erg s^{-1} cm^{-2}. Among them, 16 [O II] emitters in the central region of the cluster are confirmed by near-infrared spectroscopy with Subaru/MOIRCS, suggesting that our photometric selection is valid to sample [O II] emitters at $z = 1.46$. We find that [O II] emitters are distributed along filamentary large-scale structures around the cluster, which are among the largest structures of star-forming galaxies ever identified at $1.3 \lesssim z \lesssim 3.0$. We define several environments such as cluster core, outskirts, filament, and field, in order to investigate the environmental dependence of star-forming galaxies at $z = 1.46$. The colour–magnitude diagram of $z' - K$ vs. K for the [O II] emitting galaxies shows that a significantly higher fraction of [O II] emitters with red $z' - K$ colours is seen in the cluster core than in other environments. It seems that the environment which hosts such red star-forming galaxies shifts from the core region at $z = 1.46$ to the outskirts of clusters at lower redshifts. The multi-colour analysis of the red emitters indicates that these galaxies are more like nearly passively evolving galaxies which host [O II] emitting AGNs, rather than dust-reddened star-forming [O II] emitters. We argue therefore that AGN feedback may be one of the critical processes to quench star formation in massive galaxies in high density regions. The emission line ratios of [O III]/Hβ and [N II]/Hα of the [O II] emitters in the cluster core support that there is a moderate contribution of AGN to the emitters. We also find that the cluster has experienced high star formation activities at rates comparable to that in the field at $z = 1.46$ in contrast to lower redshift clusters, and that star formation activity in galaxy clusters on average increases with redshift up to $z = 1.46$. In addition, line ratios of [N II]/Hα and [O III]/Hβ indicate that a mass–metallicity relation exists in the cluster at $z = 1.46$, which is similar to that of star-forming galaxies in the field at $z \sim 2$. These results all suggest that at $z \sim 1.5$ star formation activity in the cluster core becomes as high as those in low density environments and there is apparently not yet a strong environmental dependence, except for the red emitters.

Key words: galaxies: clusters: general – galaxies: clusters: individual: XMMXCS J2215.9-1738 – galaxies: evolution.

1 INTRODUCTION

Recently, galaxy clusters at high redshift of $z > 1$, especially $z \gtrsim 1.5$, are found one after another (Kurk et al. 2009; Papovich et al. 2010; Tanaka et al. 2010; Henry et al. 2010; Gobat et al. 2011; Fassbender et al. 2011). These high-z clusters provide important clues to understanding galaxy formation and evolution, since the redshift of $z > 1$ approaches the epoch when galaxy clusters were formed. The importance of $z \gtrsim 1$ on galaxy evolution is also supported by the fact that the cosmic star formation activity and the number density of active galactic nuclei (AGN) both come to a peak at z=1–3

⋆ E-mail: masao.hayashi@nao.ac.jp

© 2011 RAS

(e.g., Ueda et al. 2003; Hopkins & Beacom 2006), and this redshift range corresponds to the epoch when galaxies and AGNs are evolving vigorously. In galaxy clusters at low and intermediate redshifts of $z < 1$, a prominent sequence of red galaxies is seen in a color-magnitude diagram (e.g., Bower et al. 1992; Kodama et al. 1998; Stanford et al. 1998; van Dokkum et al. 1998; Blakeslee et al. 2003; Tanaka et al. 2005; De Lucia et al. 2007). It is also well-known that clusters are dominated by early-type galaxies. On the other hand, in proto-clusters at high redshift of $z > 3$, overdense regions of star-forming galaxies such as Lyman alpha emitters and Lyman break galaxies are reported (e.g., Steidel et al. 1998). Kodama et al. (2007) found a deficit of massive galaxies on red sequence in proto-clusters at $z \sim 3$, while such red galaxies are already in place in proto-clusters at $z \sim 2$ (see also Kajisawa et al. 2006; Kriek et al. 2008; Doherty et al. 2010). These results suggest that the blue star-forming galaxies in the early phase evolve to red passive galaxies in high density regions during the redshift interval of 1–3. In fact, recent studies show that clusters at $z \gtrsim 1.5$ are conducting active star formation even in the core regions (Hayashi et al. 2010; Hilton et al. 2010; Fassbender et al. 2011; Papovich et al. 2010; Tran et al. 2010). It is thus important to reveal star formation and AGN activities in galaxy clusters at this epoch.

An effective method of selecting star-forming galaxies is to search for emission line galaxies based on narrow-band imaging, which enables us to sample star-forming galaxies with line emission stronger than a certain limiting flux and an equivalent width. A wide-field imaging is also essential to cover cluster outskirts and surrounding field regions as well as cluster cores for environmental studies. Recent studies have discovered that the medium-density regions in the outskirts of galaxy clusters are the key environment to determine galaxy properties such as colours and star formation activities during the course of cluster assembly (Tanaka et al. 2005; Koyama et al. 2008). They found that the colours of galaxies change sharply from blue to red in such medium-density regions. Furthermore, Koyama et al. (2008) found that it is possible that star formation is the most active in the medium-density regions at $z = 0.81$. These studies have demonstrated the importance of wide-field surveys comprehensively covering all the range in environments from cluster cores to the surrounding fields.

Moreover, follow-up spectroscopy of the emitters detected in the narrow-band imaging is essential to characterize their detailed properties such as dust-corrected star formation rate (SFR), AGN contribution and gaseous metallicity. At $z = 1 - 3$, because all the useful emission lines such as Hα, Hβ, and [O III] are redshifted into the near-infrared regime, deep multi-object near-infrared (NIR) spectroscopy becomes critically important and effective. Dust correction is one of the major uncertainties in characterizing galaxy properties from the observed data, and the Balmer decrement measurement (Hβ/Hα) with NIR spectroscopy is essential to make accurate correction for dust extinction. Moreover, recent NIR spectroscopic observations of star-forming galaxies at high redshifts have revealed that there is a mass–metallicity relation up to $z \sim 3$, and that the chemical evolution is seen in the sense that galaxies with a given stellar mass have lower metallicities on average with increasing redshift (Maiolino et al. 2008; Mannucci et al. 2009). More recently, Mannucci et al. (2010) discovered a fundamental relationship between stellar mass, metallicity, and SFR, which indicates that galaxies with smaller stellar masses and/or higher SFRs have lower metallicities. It should be noted that metallicities of galaxies also depend on the sample selection (e.g., Hayashi et al. 2009; Yoshikawa et al. 2010; Onodera et al. 2010). All these previous studies were, however, conducted in general fields, and it is yet unknown whether such mass–metallicity relation is established in clusters and how it depends on environment. Metallicity of star-forming galaxies provides information on the integrated star formation history in galaxies and it is independent from the snap-shot measurement of on-going star formation rate at each epoch. Therefore, the NIR spectroscopy of star-forming galaxies in various environments at $z > 1$ is the key to understanding galaxy evolution and its environmental dependence in much greater detail.

We have been conducting deep and wide-field surveys of Hα and [O II] emitters in some general fields and in galaxy clusters at various redshifts at $z > 0.4$ as MAHALO-Subaru project (MApping HAlpha and Lines of Oxygen with Subaru; PI is T. Kodama). Among the clusters targeted by our project, XMMXCS J2215.9-1738 cluster (hereafter XCS2215 cluster) at $z = 1.46$ (Stanford et al. 2006) is one of the most massive galaxy clusters at high redshift of $z > 1$. Hayashi et al. (2010) reported a deep survey of [O II] emitters in the central $6' \times 6'$ region of the XCS2215 cluster, and found that there are a lot of star forming galaxies even in the cluster core where almost no star formation is seen in lower-z clusters. Hilton et al. (2010) found eight mid-infrared (24μm) sources in the central region of the XCS2215 cluster with Spitzer/MIPS, which supports our results that a relatively large fraction of galaxies in the XCS2215 cluster are still having active star formation. The previous [O II] survey (Hayashi et al. 2010) was limited to the central $6' \times 6'$ area where we had the MOIRCS K_s-band data as well. In this paper, we expand our previous survey to the outskirts of this cluster in order to investigate the environmental dependence of galaxy properties at $z = 1.46$. Our new UKIRT wide-field K-band imaging data now enable us to perform the analysis over the full Suprime-Cam field across ~30 arcmin in diameter. At the same time we perform follow-up NIR spectroscopy of [O II] emitters identified in the central region of the cluster to examine their properties in detail.

The structure of this paper is as follows. Observations and available data for the XCS2215 cluster are described in § 2. Then, [O II] emitters at $z = 1.46$ around the cluster are selected from the photometric catalogues in § 3. Some of the [O II] emitters are confirmed by spectroscopy in § 4. In § 5, environmental dependence of colour, SFR, and specific SFR are discussed, and we compare the star forming activity of this cluster to those of lower-z clusters in § 6. In § 7, we investigate AGN contribution, dust extinction, and gas-phase metallicity based on the emission line ratios between Hα, Hβ, [O III], and [N II] lines. Finally, in § 8, we summarize our results of this paper and make conclusions. Throughout this paper, magnitudes are presented in the AB system, and we adopt cosmological parameters of $h = 0.7$, $\Omega_m = 0.3$ and $\Omega_\Lambda = 0.7$. Vega magnitudes in J and K, if preferred, can be obtained from our AB magnitudes using the relations: J(Vega)=J(AB)−0.92 and K(Vega)=K(AB)−1.90, respec-

Table 1. Summary of the optical and NIR imaging data. The limiting magnitudes are measured with a 2″diameter aperture. Note that J-band data are available only in the central region of the cluster, and its depth depends on the position due to non-uniform integration times. The PSFs in all the co-added images are matched to 1.09 arcsec.

filter	effective area (arcmin^2)	net integration (minutes)	limiting mag. (3σ)	instrument	observation date
B	32×23	140	27.6	Subaru/Suprime-Cam	2008/07/30-31†
R_c	32×23	88	27.1	Subaru/Suprime-Cam	2009/07/20
i'	32×23	90	26.8	Subaru/Suprime-Cam	2009/07/20
z'	32×23	80	25.8	Subaru/Suprime-Cam	2008/07/30-31†
NB912	32×23	260	25.8	Subaru/Suprime-Cam	2008/07/30-31†
J	6×6	32.5 – 92.3	23.8 – 24.6	Subaru/MOIRCS	2007/08/07‡, 2008/06/29-30†
K	32×23	123	23.4	UKIRT/WFCAM	2010/07/30-31

† Hayashi et al. (2010), ‡ Hilton et al. (2009)

tively. In $z = 1.46$, 1 arcmin corresponds to 1.25 Mpc (comoving) and 0.51 Mpc (physical), respectively.

2 OBSERVATIONS AND DATA

2.1 Optical imaging data

We have obtained optical imaging data of the XCS2215 cluster with Subaru Prime Focus Camera (Suprime-Cam; Miyazaki et al. 2002) on the Subaru telescope. Suprime-Cam consists of ten 2048×4096 CCDs with a pixel scale of 0.20″, and has a wide field-of-view (FoV) of 34×27 arcmin^2, which enables us to cover from the central region to the outskirts of the cluster by a single pointing. Our multi-wavelength data set consists of four broad-band images in B, R_c, i', z' bands, and a narrow-band image of NB912 (λ_c=9139Å, $\Delta\lambda$=134Å).

The observations were conducted in two semesters. The B, z', and NB912-band imaging were performed under a normal open-use program (S08A-011, PI: T. Kodama) on 2008 July 30-31, while R_c and i'-band imaging were performed under a service-mode open-use program (S09A-168S, PI: M. Hayashi) on 2009 July 20. The details of the observation and data reduction for B, z' and NB912 data are described in Hayashi et al. (2010). In this paper, therefore, we mainly describe the additional data in R_c and i'. The individual exposure times of a frame in R_c and i' were 8 and 6 minutes, and the total integration times were 88 and 90 minutes, respectively. The weather was fine during the observations. The sky condition was mostly photometric, although thin cirrus occasionally passed the targeted location. The seeing was 0.6–0.8 arcsec in both R_c and i'.

The data reduction of R_c and i' was carried out in the same manner as for the B, z', and NB912 data, and we used the data reduction package for Suprime-Cam (SDFRED ver.1.4: Yagi et al. 2002; Ouchi et al. 2004). The point spread functions (PSFs) in the R_c and i' images were matched to 1.09 arcsec, which was the PSF size of the other optical data. The photometric zero-points were determined using the photometric standard stars in SA113 (Landolt 1992). The 3σ limiting magnitudes were 27.1 and 26.8 in R_c and i', respectively. The specifications of all the optical data are summarized in Table 1.

2.2 Near-infrared imaging data

The NIR imaging data are updated from Hayashi et al. (2010), where we had J and K_s-band data covering only the central 6′×6′ region with Multi-Object Infrared Camera and Spectrograph (MOIRCS; Ichikawa et al. 2006; Suzuki et al. 2008) on the Subaru telescope. MOIRCS consists of two 2048×2048 HgCdTe detectors with a pixel scale of 0.117″, and its FoV is 4′×7′.

We have now obtained a new wide-field K-band data with Wide Field Camera (WFCAM; Casali et al. 2007) on the United Kingdom Infrared Telescope (UKIRT) on 2010 July 30–31 (U/10A/J3, PI: Y. Koyama) in order to cover the entire region of the optical data. WFCAM consists of four 2048×2048 HgCdTe detectors with a pixel scale of 0.4″, and each detector can cover 13.65′×13.65′ region. Because the detectors are spaced with a gap of 12.83′, four pointings are required to get a contiguous sky coverage of a 0.75 square degrees. A dither pattern of five points with 2×2 small microstepping was set for each pointing, and so the individual exposures were conducted at 20 different positions for a cycle at each pointing. The exposure time of each frame was 10 seconds, and the total integration time at each pointing was 123 minutes. The weather was fine throughout the two days of the observing run, and the sky condition was photometric. The seeing was ∼1.0 arcsec.

We reduced the WFCAM data in a standard manner using our own IRAF-based software (provided by K. Motohara). First, we subtracted a dark frame from individual object frames, and then a self-flat image was created by combining 80 frames (4 cycles) and taking a median value at each pixel. After flat-fielding, all the object frames were temporarily mosaiced and co-added. We then conducted a source detection on the co-added image. Next, after masking the detected objects in the individual frames, we make self-flat images again, and then conduct a flat-fielding per each observation cycle of 20 frames. After the sky background was subtracted from each frame, 20 frames of each cycle are combined. Finally, PSF sizes of the images of each cycle are matched, and the frames were mosaiced and co-added to make the final images. A special care was taken to exclude spurious objects due to crosstalk of bright objects. PSF in K was matched to 1.09 arcsec. The photometric zero-point was determined with 2MASS catalog (Skrutskie et al. 2006).

Table 2. Summary of the spectroscopic observations with Subaru/MOIRCS.

slitmask	# of target	grism	integration (minutes)	seeing (arcsec)
MOS1	17	$zJ500$	180	0.55-0.80
MOS2	17	$zJ500$	300	0.45-0.60

The 3σ limiting magnitude was 23.3 in K. The specifications of the NIR data are also summarized in Table 1

For J-band, we added the archival data with MOIRCS by Hilton et al. (2009) to our own data. Hilton et al. (2009) observed a $4' \times 4'$ region of the cluster core with the chip 2 only of MOIRCS with an exposure time of 1485 seconds in total. Combining the archive data with our own data, we conducted the data reduction again in the same manner as in Hayashi et al. (2010) using the data reduction package for MOIRCS (MCSRED[4] by I. Tanaka et al.). PSF in J was matched to 1.09 arcsec.

2.3 Near-infrared spectroscopic data

We conducted a follow-up NIR spectroscopy of [O II] emitters in the central region of the cluster with MOIRCS on the Subaru telescope on 2009 September 3–7 (S09B-012, PI: T. Kodama). For 34 out of 44 [O II] emitter candidates identified in Hayashi et al. (2010), we obtained NIR low-resolution spectra with $zJ500$ grism with a resolution of $R = 700$ at J-band and a wavelength coverage of 0.9–1.8μm. The dispersion was 5.57 Å pixel^{-1}. We used two masks, and 17 slits were allocated to the [O II] emitter candidates in each mask. The width and the length of individual slits were $0.7''$and 11-12$''$, respectively. Depending on the positions of slits on the mask, 24 spectra have a wavelength coverage of 1.0–1.7μm, which can neatly cover all the redshifted Hα, Hβ, [O III], and [N II] emission lines if present. The remaining 10 spectra have a coverage of 1.0–1.35μm, which covers Hβ, and [O III] emission lines. Moreover, about two-thirds of the spectra, i.e. 21 [O II] emitters, extend down to 0.9μm. The specifications of the spectroscopic observations are summarized in Table 2.

We observed the targets consecutively at two positions (A and B) with a offset of $3''$ on the slit. Single exposure time was 600 or 900 seconds depending on the sky background level. The total on-source integration time was 3 hours for the MOS1 mask and 5 hours for the MOS2 mask. We also observed a standard star BD+17°4708 (Bohlin & Gilliland 2004) on each night to correct for a telluric absorption as well as the instrumental efficiency, and to make flux calibration. Most of the time during the observations, however, the weather condition was not good and the sky was covered with thin cirrus and not photometric. Therefore, the absolute flux calibration was very difficult for these spectra. The seeing was 0.45–$0.80''$in FWHM.

The data reduction was done with standard procedures using IRAF. First, bad pixels and cosmic rays were removed from each frame, and a A$-$B frame was created from a pair of successive frames observed at the two positions A and B. Then, flat-fielding was done with a dome-flat image for the individual A$-$B images. Next, distortion was corrected using a calibration data provided by the MOIRCS instrument team. After extracting a spectrum at each slit, wavelength calibration was done with the OH airglow lines. Then, residual sky subtraction was carried out, since the A$-$B procedure alone might not completely remove the sky background due to its time variation. All the spectra for each [O II] emitter were then co-added and an one-dimensional spectrum was extracted by combining ten pixels along a slit. Finally, the telluric absorption and the instrumental efficiency were corrected using the spectra of BD+17°4708. As an error, the sky noise was estimated as a square root of the photon count on the sky spectrum.

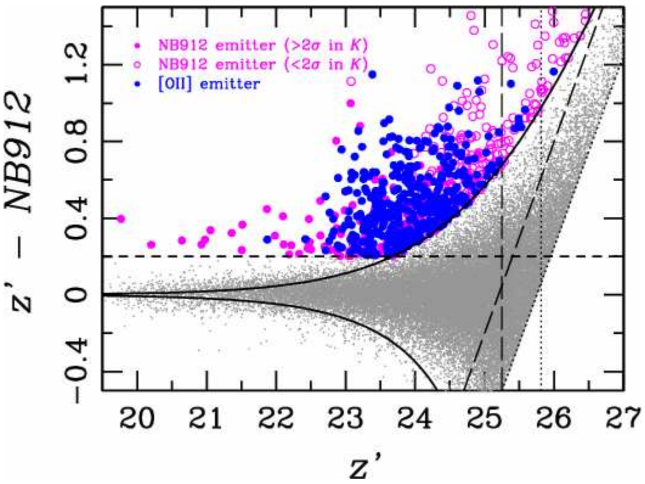

Figure 1. colour–magnitude diagram of z' vs. $z' - NB912$. Solid lines show 3σ excesses of $NB912$ over z'. Long-dashed and dotted lines show 5σ and 3σ limiting magnitudes, respectively. Short-dashed line shows $z' - NB912 = 0.2$. Gray dots show galaxies brighter than 5σ in NB912. Magenta filled circles indicate NB912 emitters with more than 2σ detections in K, while magenta open circles indicate those without detection in K. Blue filled circles show our 380 [O II] emitters in the XCS2215 cluster.

2.4 Photometric catalogue

We make a photometric catalogue in the same manner as in Hayashi et al. (2010), but for the wide-field 32×23 arcmin^2 data instead of the central 6×6 arcmin^2 region of the cluster. In this section, we briefly describe our updated photometric catalogue.

Source detections are performed on the NB912 image using SExtractor (ver. 2.5.0: Bertin & Arnouts 1996), and photometry on the other images, except for the J-band, are conducted by the double-image mode of SExtractor. Because the FoV of the J-band image is limited to the central region and the pixel scale of MOIRCS image is smaller than that of Suprime-Cam, the J image is not matched to the NB912 image geometrically. Therefore, we independently conduct source detections and photometry on the J image with SExtractor, and cross-match the detected objects to those in the NB912-detected catalogue if the coordinates of

---

[4] http://www.naoj.org/staff/ichi/MCSRED/mcsred.html

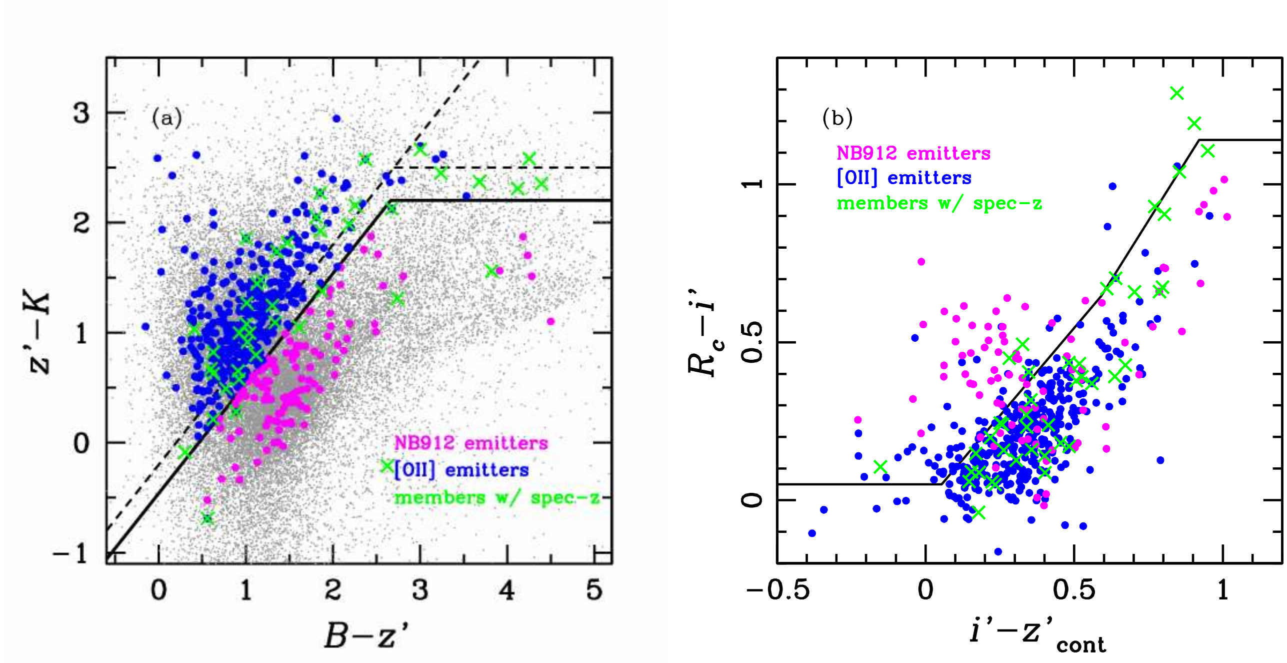

Figure 2. (a) Left panel: the colour-colour diagram of $B - z'$ vs. $z' - K$. The solid lines show our criteria for the selection of [O II] emitters at $z \sim 1.46$, while the broken lines indicate the original BzK selection criteria defined by Daddi et al. (2004). Blue filled circles show 380 [O II] emitters, and magenta filled circles show NB912 emitters other than [O II] emitters. Gray dots are galaxies brighter than 5σ detection in NB912, and green crosses indicate cluster members confirmed by our MOIRCS spectroscopy and Hilton et al. (2010). (b) Right panel: the colour-colour diagram of $i' - z'_{\rm cont}$ vs. $R_c - i'$ for the [O II] emitters and the other NB912 emitters which are identified based on the $Bz'K$ diagram (see the left panel). Note that in this plot, H α emitters at $z = 0.39$ have already been excluded based on $R_c - i'$ and $B - R_c$ colours. Symbols are the same as in the left panel. Solid lines show the criteria used in Ly et al. (2007).

the J-detected objects are in agreement with those of the NB912-detected objects within a 1″-diameter circle. Colour indices are derived from the 2″-diameter aperture magnitudes, and MAG_AUTO magnitudes are used as total magnitudes. Magnitude errors are estimated from 1σ sky noise taking account of the difference in depth at each object position due to slightly different exposure times and sensitivities. Magnitudes are corrected for the Galactic absorption by the following magnitudes; A(B)=0.10, A(R_c)=0.06, A(i')=0.05, A(z')=0.04, A(NB912)=0.04, A(J)=0.02, and A(K)=0.01, which are derived from the extinction law of Cardelli et al. (1989) on the assumption of $R_V = 3.1$ and $E(B-V) = 0.025$ estimated from Schlegel et al. (1998). We check the zero-points of magnitudes in all the bands by comparing stellar colours with those of stellar spectrophotometric atlas of Gunn & Stryker (1983). The zero-point magnitudes are corrected so that stellar colours are in good agreement with those of the stellar atlas. Note that the correction is smaller than 0.15 magnitude at most.

As a result, the catalogue contains 31,144 objects brighter than 25.20 mag. in NB912 (5σ limiting magnitude) over the whole 32×23 arcmin^2 region, except for the masked regions. Among them, 27,430 galaxies are distinguished from 3,714 stars based on $B-z'$ and $z'-K$ colours. This technique was devised by Daddi et al. (2004), and stars are actually well separated from galaxies on this colour-colour diagram ($B - z'$ vs. $z' - K$) (Daddi et al. 2004; Kong et al. 2006).

3 SELECTION OF [O II] EMITTERS

We already surveyed [O II] emitters in the central region of the XCS2215 cluster at $z = 1.46$ with a combination of $NB912$ and z'-bands, and identified 44 [O II] emitters (Hayashi et al. 2010). In this paper, we have expanded the survey area to the outskirts of the cluster applying the same technique used in Hayashi et al. (2010). We thus only describe a summary of our selection method below.

First, we select galaxies with a emission line at ∼9139Å by applying the following criteria;

$$\text{(i)}\ \ z' - NB912 \geqq -2.5\log(1 - \sqrt{f^2_{3\sigma,z'} + f^2_{3\sigma,NB912}}/f_{z'}),$$

$$\text{(ii)}\ \ z' - NB912 \geqq -0.2,$$

where $f_{3\sigma}$ is the 3σ sky noise flux in each band and $f_{z'}$ is the z'-band flux (Fig. 1). The first criterion is intended to select galaxies with an excess in $z' - NB912$ colour redder than the 3σ photometric error. This corresponds to a line flux larger than 1.4×10^{-17} erg s^{-1} cm^{-2}. If the excess is due to a [O II] emission line at $z = 1.46$, the limiting flux corresponds to a dust-free SFR of 2.6 M$_\odot$ yr^{-1} according to the [O II]–SFR calibration in Kennicutt (1998). The second criterion corresponds to the observed equivalent width larger than 35Å, which can exclude the possible contamination of galaxies due mainly to photometric errors. As discussed in Hayashi et al. (2010), the colour term in $z' - NB912$ is negligible. As a result, we select 721 NB912 emitters from 27,430 galaxies over a ∼700 arcmin^2 area (Fig. 1). Among them, 482 emitters are detected in K at more than 2σ level. In what follows, we deal with the K-detected emitters, because we

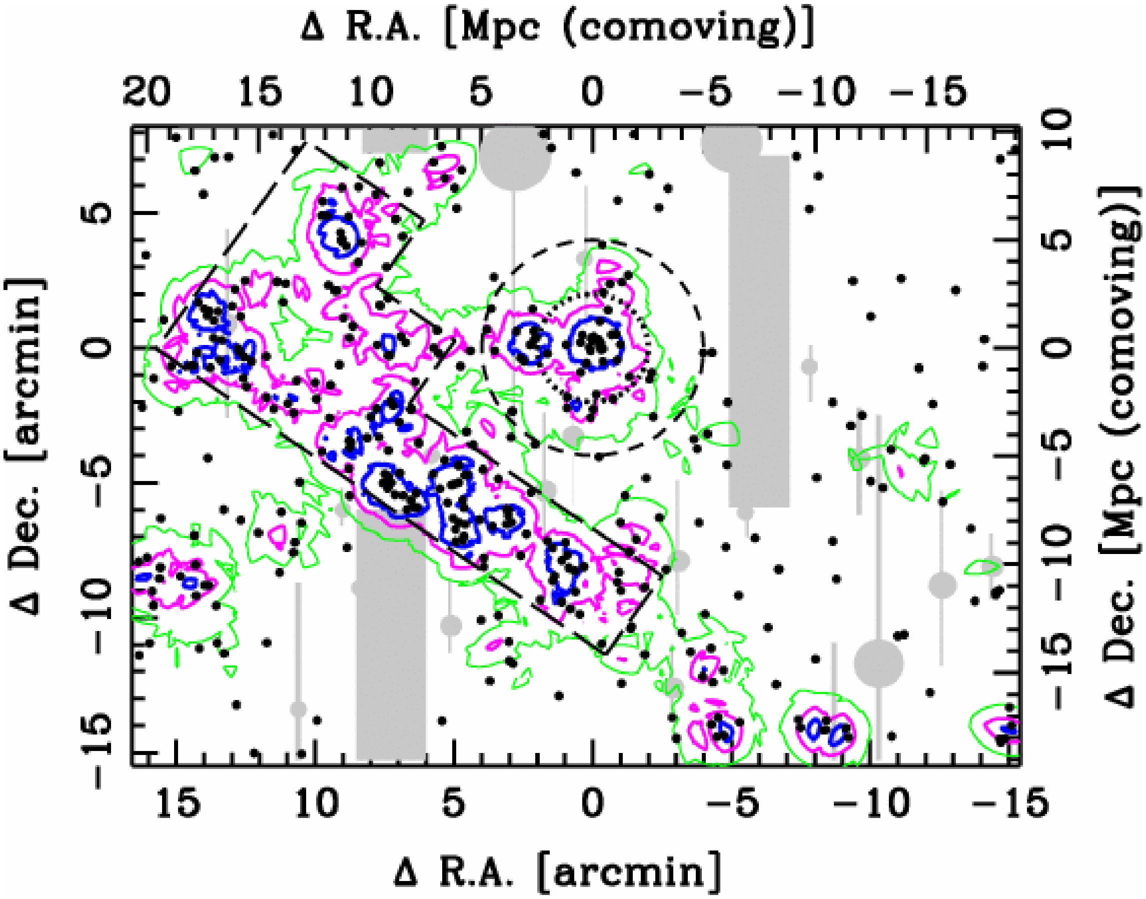

Figure 3. The celestial distribution of our 380 [O II] emitters at $z \sim 1.46$ in and around the XCS2215 cluster. North is up, and east is to the left. The horizontal and vertical axes show relative coordinates from the cluster centre. Black dots show the [O II] emitters, and gray regions indicate the masked areas around bright stars which have bad quality image and were excluded from the analyses. Cluster core region is defined by a dotted-line circle with a radius of $2'$, while outskirts region is defined as a ring with a width of $2'$ between the dotted and broken-line circles. Filament region shown by the long-dashed lines is defined to cover the prominent structure of the [O II] emitters. The rest of the area is defined as the field. Blue, magenta and green contours show the local density of $\log\Sigma_{5\mathrm{th}}[\mathrm{Mpc}^{-2}]$ =1.07, 0.72, and 0.39, respectively (see §5.1).

identify the [O II] emitters based on their $B-z'$ and $z'-K$ colours. This means that our emitter sample is both flux- and mass-limited.

It is possible that the detected emission lines are any of the following major strong lines; H α at z=0.39, [O III] at z=0.82–0.84, H β at z=0.88, and [O II] at z=1.46. Note that we find no candidates for Lyα emitters at z=6.51 in our sample, because our 482 NB912 emitters are all detected in i'-band. In order to discriminate [O II] emitters from other lines at different redshifts, we apply the colour selection criteria to the NB912 emitters;

$$(z'_{\rm cont}-K) > (B-z'_{\rm cont}) - 0.46 \;\cup\; (z'_{\rm cont}-K) > 2.2, \quad (1)$$

where $z'_{\rm cont}$ corresponds to a continuum flux calculated from equation (3) in §5.3. The original idea comes from Daddi et al. (2004) who devised the BzK colour selection technique which can efficiently take out galaxies located between $1.4 < z < 2.5$. We modified the original selection boundaries in Hayashi et al. (2010) so that we can sample galaxies at $z = 1.46$ more completely. Note that the selection criteria (1) used in this paper are yet slightly different from those adopted in Hayashi et al. (2010). Firstly, we use $z'_{\rm cont}$ instead of z', which enables us to remove a contribution of emission line to the continuum colour to be used in the colour selection. The other is that we use K magnitudes taken with WFCAM/UKIRT instead of K_s magnitude with MOIRCS/Subaru. We estimate K_s(MOIRCS)$-K$(WFCAM) colours using spectral templates of Coleman et al. (1980) which are redshifted to 1.46, and find that the difference of the filters can result in K_s(MOIRCS)$-K$(WFCAM)=0.02–0.05. This works in the sense that the emitters close to the border tend to meet the criteria more easily.

With the above criteria, we select 376 [O II] emitters in total (Fig. 2(a)). In Hayashi et al. (2010), we identified 44 [O II] emitters in the central region of the cluster. We check whether these previous sample of [O II] emitters are reproduced in the current sample in this paper. Among the 44 [O II] emitters, however, 11 objects are not identified as [O II] emitters in the current sample. This is because of the update of photometric catalogue in particular in the K-band. The MOIRCS K_s image used in Hayashi et al. (2010) is ~ 0.3 mag. deeper than the WFCAM K image, and we miss some [O II] emitters with faint K magnitudes. In fact, seven ob-

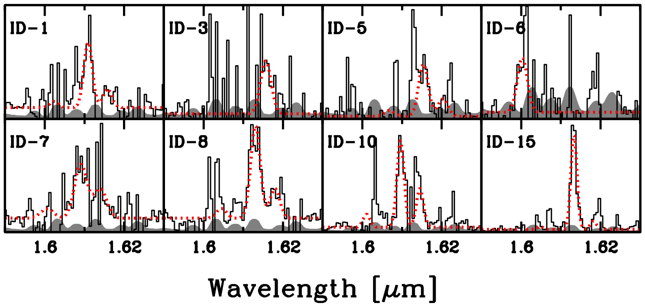

Figure 4. Spectra of the [O II] emitters which show H α and [N II] emission lines, except for ID-3 and ID-6 where only H α lines are detected. They cover a wavelength range of 1.59–1.63μm in the observed frame. The vertical axis is flux density in arbitrary unit. The solid lines show the spectra, and the gray regions show 1σ errors. Gaussian profiles are fitted to the lines and are shown by the red dotted lines together with the continuum levels.

jects out of 11 are not detected in the WFCAM K imaging. However, for an uniformity of the data across the entire field, we use the WFCAM data in this paper. Hilton et al. (2010) have spectroscopically confirmed 44 member galaxies in the XCS2215 cluster. We have also confirmed membership for 16 [O II] emitters with spectroscopy (see § 4). Among them, four NB912 emitters do not meet our [O II] selection criteria but they turn out to be real members at $z \sim 1.46$. We thus add them to our [O II] emitter sample. Consequently, our final [O II] emitter sample consists of 380 galaxies.

Ly et al. (2007) have classified emission line galaxies using only the optical colours. We test this selection method based on $R_c - i'$ vs. $B - R_c$ and $i' - z'$ vs. $R_c - i'$ diagrams used in Ly et al. (2007) and check whether it is effective in picking out [O II] emitters at $z \sim 1.46$. If this classification works, we could select [O II] emitters among those faint in K magnitude, i.e. less massive star-forming galaxies. Fig. 2(b) shows $i' - z'$ and $R_c - i'$ colours for [O II] and the other NB912 emitters identified by the $Bz'K$ selection method, where H α emitters at $z = 0.39$ have already been excluded from the NB912 emitter sample based on the $R_c - i'$ vs. $B - R_c$ colours (Ly et al. 2007). In Fig. 2(b), it seems that [O II] emitters and the spectroscopically confirmed members are relatively well distinguished and confined mostly in the bottom-right side of the diagram (Ly et al. 2007). However, we also note that there are many contaminations from other lines at different redshifts. This suggests that the NIR data is essential to photometrically select galaxies at $z \sim$1–2, and we decide not to use the optical colour selection.

Also, we calculate photometric redshifts using the EAZY code (Brammer et al. 2008) with six SED templates of EAZY_v1.0 and based on the photometry in B, R_c, i', z' and K bands for the K-detected subsample of spectroscopic members. However, 20% of the spectroscopic members have completely wrong photometric redshifts at $z_{\rm phot} < 1$. Therefore we do not use the photometric redshift technique either.

Therefore, in this paper, we will rely on the $Bz'K$ colour selection in identifying the [O II] emitters at $z \sim 1.46$ among the NB912 emitters.

Fig. 3 shows the distribution of [O II] emitters at $z \sim 1.46$, where gray regions are masked due to bad quality of the image. We confirm that many [O II] emitters exist in the central region, as is already reported in Hayashi et al. (2010). Moreover, due to the extension of our survey to the outskirts of the XCS2215 cluster, we also find that there is a prominent filamentary large-scale structure of [O II] emitters from the east to the south of the cluster (Fig. 3). This filament is surely one of the largest structures of star-forming galaxies at $z = 1.46$. Recent studies suggest that at lower redshifts medium-density regions embedded in large-scale structures surrounding clusters are crucial sites to understand galaxy evolution (Tanaka et al. 2005; Koyama et al. 2008). The discovery of the large-scale structure at $z = 1.46$ provides us with a unique opportunity to investigate environmental dependence of galaxy properties in particular those in such interesting medium-density environments at this high redshift. In §5, we examine the properties of galaxies in the filamentary structure, and compare them with those in different environments.

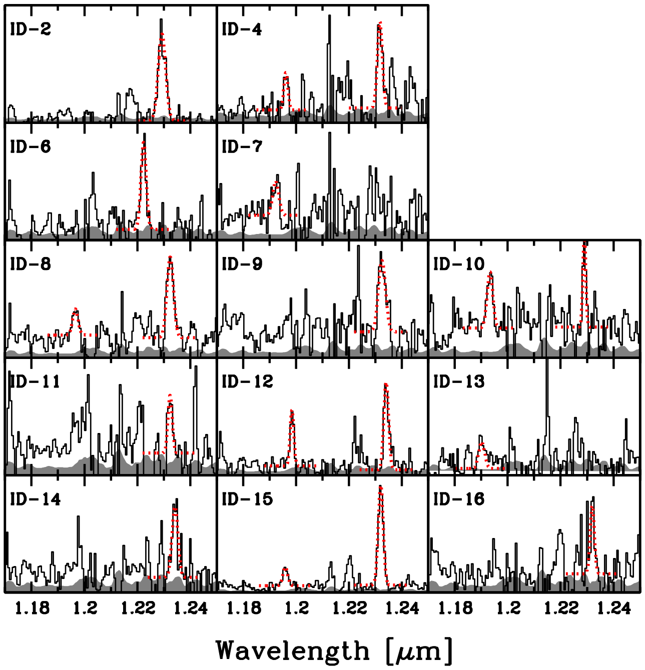

Figure 5. Same as Fig. 4, but for H β and [O III] emission lines. The spectra cover a wavelength range of 1.17–1.25μm in the observed frame. Gaussian profiles with continuum levels are shown wherever the H β and/or [O III](λ5007) are detected.

4 SPECTROSCOPIC CONFIRMATION OF THE [O II] EMITTERS

In Hayashi et al. (2010) and the previous section, we photometrically identify 380 [O II] emitters at $z = 1.46$ in the XCS2215 cluster and its outskirts. However, the confirmation of [O II] emitters by spectroscopy is essential to verify that our method is valid for the selection of [O II] emitters at $z = 1.46$.

By our MOIRCS spectroscopy, we have detected some emission lines, such as H α, H β, [O III], [N II], for 16 out of the 34 targeted [O II] emitters in the cluster region. In the case of narrow-band emitters, it is relatively easy to identify the detected emission line even if only a single line

Table 3. A catalogue of the spectroscopically confirmed [O II] emitters.

ID	Slitmask	R.A.	Dec.	Redshift	Magnitude and Colour†			Emission lines‡				
					K_s	$B - z'$	$z' - K_s$	[O II]	H β	[O III]	H α	[N II]
1	MOS1	22:15:57.22	-17:37:53.25	1.455	21.20	1.91	2.04	—	×	×	○	○
2	MOS1	22:15:58.84	-17:38:10.07	1.455	20.91	1.37	1.67	—	×	○	×	×
3	MOS1	22:15:52.89	-17:39:08.10	1.462	20.97	1.09	1.24	—	×	×	○	×
4	MOS1	22:16:09.00	-17:38:32.66	1.460	22.01	1.03	1.03	○	○	○	—	—
5	MOS1	22:16:02.54	-17:37:56.45	1.461	22.51	1.47	1.60	×	×	×	○	○
6	MOS1	22:15:56.86	-17:35:58.52	1.440	22.86	0.89	0.94	○	×	○	○	×
7	MOS2	22:15:57.69	-17:37:45.77	1.452	20.22	2.50	2.72	—	○	×	○	○
8	MOS2	22:16:02.40	-17:39:53.35	1.460	20.98	1.31	1.54	○	○	○	○	○
9	MOS2	22:15:57.39	-17:37:04.11	1.461	21.47	1.42	1.20	○	×	○	×	×
10	MOS2	22:15:57.18	-17:38:07.88	1.454	21.68	1.15	1.28	—	○	○	○	○
11	MOS2	22:16:07.43	-17:37:25.22	1.461	21.99	1.22	1.08	○	×	○	—	—
12	MOS2	22:16:07.63	-17:36:35.68	1.465	22.51	0.71	0.58	○	○	○	—	—
13	MOS2	22:15:56.90	-17:38:33.88	1.448	22.64	0.63	1.51	○	○	×	×	×
14	MOS2	22:15:49.50	-17:38:58.35	1.465	22.79	0.67	0.79	○	×	○	—	—
15	MOS2	22:15:59.46	-17:38:37.61	1.460	22.80	0.71	0.26	—	○	○	○	○
16	MOS2	22:16:08.05	-17:37:55.95	1.461	23.19	0.78	0.78	○	×	○	—	—

† Magnitudes and colours are taken from the catalogue of Hayashi et al. (2010).
‡ ○: detected, ×: not detected, —: no data

is detected on the spectrum. Because we already detect a emission line at ~ 9139Å by narrow-band imaging, the possible redshifts of the emitters are very limited. For [O II] emitters at $z = 1.46$, H α and [N II] lines should be seen at $\lambda \sim$1.61µm, while H β and [O III] lines should be seen at $\lambda \sim$ 1.19µm and 1.23µm, respectively.

We first perform line detections in the two-dimensional spectra by visual inspection, taking care not to be confused by residual OH airglow lines or any accidental noises. Among the confirmed lines, we then regard a line with a flux larger than 2σ of the sky noise as a real signal. Figs. 4 and 5 show the one-dimensional spectra of the lines, and a summary of the detected lines for the 16 confirmed [O II] emitters is shown in Table 3.

The spectroscopic redshifts and the fluxes of the emission lines are measured by fitting Gaussian profiles, where the free parameters are amplitude, line width, and redshift. Before fitting, we estimate a constant continuum level using the regions close to the line and without a contribution of strong OH lines, and subtract it from each spectrum. The 1σ error of the spectrum is estimated from the covariance of χ^2 fitting based on the sky noise. We confirm that the error is comparable to the sum of the sky noise within 2×FWHM around each line. If a [N II] emission line is seen in a spectrum, H α and a doublet of [N II] ($\lambda\lambda 6548, 6584$) are simultaneously fit to the spectrum, assuming the same line width and redshift, and a [N II]($\lambda 6584$)/[N II]($\lambda 6548$) ratio of 3. In the case where several lines are detected for an emitter, we determine its redshift by taking an average of the redshifts measured by individual lines.

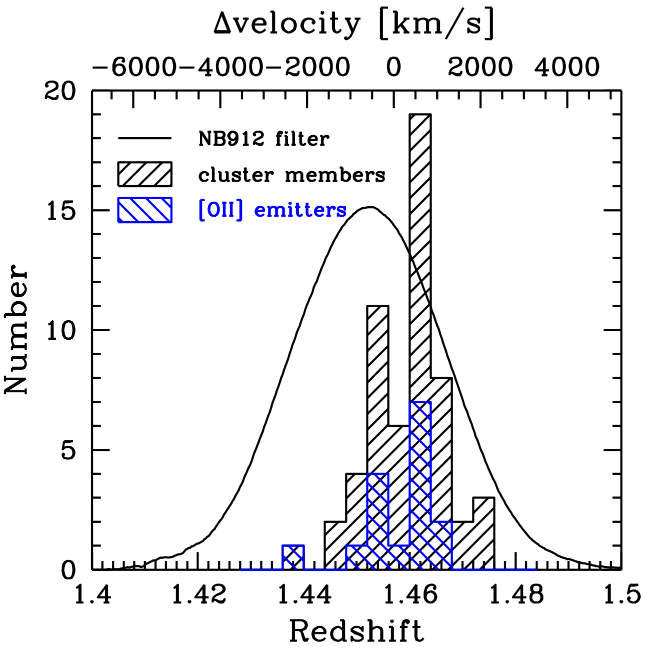

Figure 6. Redshift distributions of the cluster member galaxies. The blue histogram shows the 16 [O II] emitters which are spectroscopically confirmed by our MOIRCS observations, while the black histogram shows all the 56 members of which 40 redshifts are taken from Hilton et al. (2010). Among the 44 members in Hilton et al. (2010), four objects overlap with our [O II] emitters that are spectroscopically confirmed with MOIRCS. The solid curve shows the response function of the NB912 filter in an arbitrary unit.

As a result, we confirm that 16 [O II] emitters are certainly cluster member galaxies at $z \sim 1.46$, which is nearly 50 per cent (16/34) of our [O II] emitter sample. For other three targets, we do see an emission line at ~ 9100Å, but it is the only detected line and we are not sure whether it is an [O II] line. The spectra of two of them do not cover the wavelength where H α line should be seen, unfortunately. It is also possible that the detection limit of H α at $\sim$1.61µm is shallower than that of [O II] at $\sim$ 0.91µm. For the remaining 15 targets, no emission line is detected even if a spectrum covers the wavelength range down to 0.9µm. In

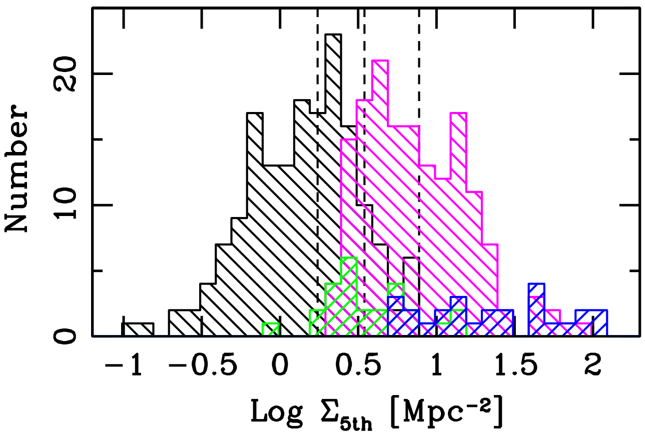

Figure 7. The histograms show the numbers of [O II] emitters as a function of the local density, $\Sigma_{5\rm th}$. Blue, green, magenta, and black histograms correspond to the core, outskirts, filament, and the field regions, respectively (see also Fig. 3). The three vertical dashed lines show the boundaries between the four environments defined based on the local density.

MOS1 (MOS2) mask, emission lines are detected for targets with [O II] fluxes larger than $0.41(0.23)\times10^{-16}$ erg s^{-1} cm^{-1} (see Table 4). We find that 12 out of the 15 targets without any line detection have estimated [O II] fluxes similar to or smaller than the limiting flux. For the two targets with estimated [O II] fluxes large enough to be detected, their spectra do not cover the wavelength range down to 0.9µm and we cannot confirm their [O II] emission lines. They do cover, however, the wavelength range up to 1.7µm where H α lines are expected to show up. But we do not detect them, either. For the remaining one target, although we obtain its spectrum covering 0.9–1.35µm, no line is detected.

Therefore, except for the three targets with strong enough estimated [O II] fluxes, non-detection of any emission lines for the [O II] emitter candidates are probably because of intrinsically too weak [O II] emission lines, as well as other lines which are also weaker than the detection limit. Non-photometric weather condition during our spectroscopy may have resulted in reducing the success rate of line detections.

Fig. 6 shows the redshift distribution of the confirmed [O II] emitters and that of all the cluster members. We cross-identify our 16 [O II] emitters to the 44 member galaxies in Hilton et al. (2010), and four galaxies turn out to be common objects whose coordinates match together to an accuracy of 1″. Hilton et al. (2010) suggest that the redshift distribution may have double peaks, and that such profile may indicate that this cluster experienced a cluster-cluster merger event within the past few Gyrs. A similar double-peaked profile is also seen for the [O II] emitters as well as all the member galaxies (Fig. 6). Although Hayashi et al. (2010) found a high fraction of [O II] emitters in the core region of the XCS2215 cluster, we were not able to reject the possibility that it is due to a projection effect of the [O II] emitters in the outskirts along the line of sight which are apparently superposed onto the cluster core. However, similarity of the redshift distributions between the [O II] emitters and all the member galaxies (Fig. 6) strongly suggests that the emitters are indeed located in the cluster core in space.

5 ENVIRONMENTAL DEPENDENCE

5.1 Definition of environments

We define four different environments (core, outskirts, filament, and the field) based on the spatial distribution of [O II] emitters as shown in Fig. 3. The core is defined as the circled region with a radius of 2′ from the cluster centre, while the outskirts is defined as the ring with an inner radius of 2′ and an outer radius of 4′. The filament is defined as the enclosed area by the long-dashed lines which neatly cover the notable filamentary structure characterized by relatively high density of the [O II] emitters. All the rest is defined as the field region.

As another definition of environment, we will also use local density $\Sigma_{5\rm th}$, which is calculated using the area where the fifth nearest [O II] emitters are included. In the local density measurements, it would be desirable to use a whole sample of $z = 1.46$ galaxies including not only blue star-forming galaxies but also red quiescent galaxies. However, the current photometric redshifts (without *J*-band in particular) are not accurate enough to define such local density of the whole population. Therefore, we count only the [O II] emitters to define local density as they are most likely located at $z = 1.46$ with little contamination from foreground or background galaxies. It should be noted that Hayashi et al. (2010) found that the fraction of [O II] emitters in this cluster is almost constant irrespective of the distance from the cluster centre. This suggests that even if only [O II] emitters are used to calculate the local density, we can expect to trace the structure of the whole population to some extent.

Fig. 7 shows the distribution of local density $\Sigma_{5\rm th}$ of the [O II] emitters in each environment defined above based on Fig. 3. If the four environments are rearranged in the order of decreasing local density, the core is the highest density region, filament is the second, the outskirts is the third, and the field is the lowest density regions. Note that the large-scale filamentary structure (i.e. filament) is actually denser than the cluster outer region (i.e. outskirts).

When we discuss environmental dependence of galaxy properties below based on the local density, we divide the galaxies into four classes according to the local densities, each of which contains an equal number of [O II] emitters ($\sim$ 95). The boundaries between the classes are shown by the two vertical dotted lines in Fig. 7.

5.2 colour–magnitude diagram

Fig. 8 shows the colour–magnitude diagrams in each environment. In the left panel the four environments are defined based on the spatial distribution of the [O II] emitters, while in the right panel the four environments are divided based on the local density (see §5.1). The distribution of the [O II] emitters on the colour–magnitude diagrams indicates that the [O II] emitters tend to be blue galaxies in general as expected. However, there are some red [O II] emitters with $z' - K > 2.2$. The fraction of the red [O II] emitters seems higher in high density regions, such as core, filament, and high-$\Sigma_{5\rm th}$ regions, compared to other environments.

Fig. 9 shows this trend quantitatively. The fraction of the red [O II] emitters ($z' - K > 2.2$) to all the [O II] emitters is plotted as a function of environment. The galaxies redder

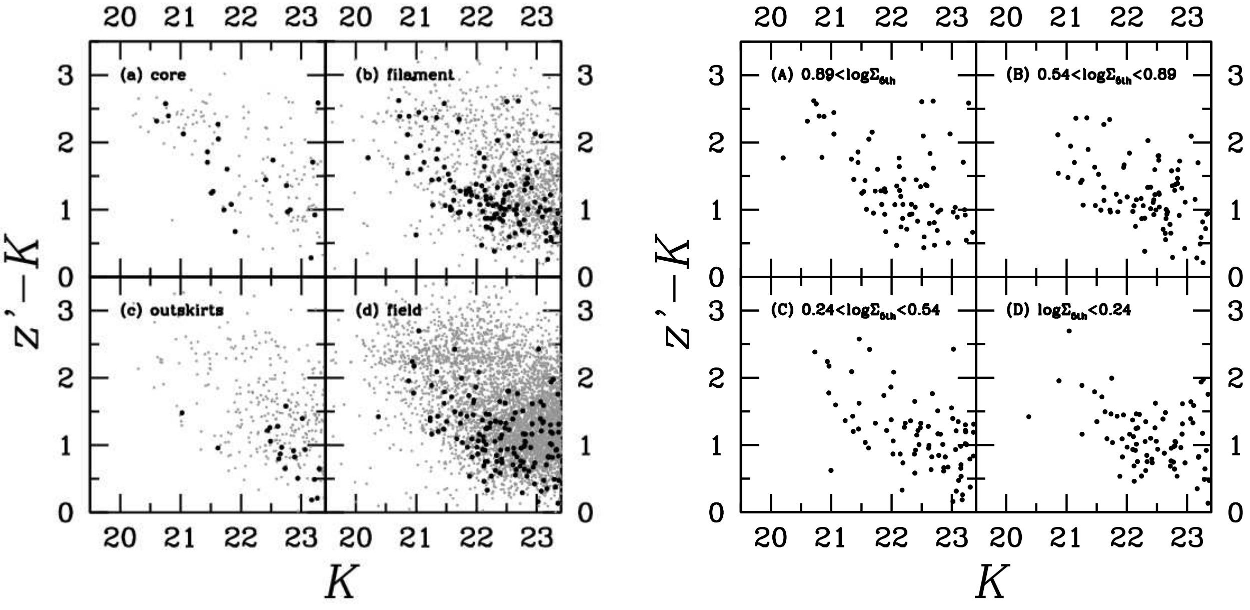

Figure 8. The $z' - K$ vs. K colour–magnitude diagram of [O II] emitters in each environment. (Left panel) Black dots are the [O II] emitters, while gray dots are the galaxies which meet colour criteria given by the equation (1). (Right panel) Same as the left panel, but the environments are separated based on the local density of $\Sigma_{5\mathrm{th}}$; (A) high density region, $0.89<\log\Sigma_{5\mathrm{th}}$, (B) medium-high density region, $0.54<\log\Sigma_{5\mathrm{th}}<0.89$, (C) medium-low density region, $0.24<\log\Sigma_{5\mathrm{th}}<0.54$, and (D) low density region, $\log\Sigma_{5\mathrm{th}}<0.24$. See text in §5.1 for the details of the four environments. Only the [O II] emitters are plotted in this panel, because the local density is calculated with the [O II] emitter sample.

than $z' - K = 2.2$ can be called as "red-sequence" galaxies for the cluster redshift at $z = 1.46$ (Hayashi et al. 2010). The figure clearly shows an excess of red [O II] emitters towards high(-est) density regions. Koyama et al. (2010) reported that such red star-forming galaxies in the RXJ1716.8+6708 cluster at $z = 0.81$ are preferentially seen in medium-density regions, such as groups, filaments, and the outskirts of the cluster, rather than in high-density cluster core. They claim that it indicates that the cluster at $z = 0.81$ has already quenched the star formation activity in the high-density region, and the region of active star formation has been shifted to the medium-density regions. Tanaka et al. (2009) also found that there are few red galaxies with [O II] emission in the RDCS J1252.9-2927 cluster at $z = 1.24$, and such galaxies tend to exist in groups or in the field. These facts may suggest that the central region of the cluster at $z = 1.46$ is at a similar stage of galaxy evolution to the outskirts of clusters at lower redshifts, where red star-forming galaxies appear.

It is clear from Fig. 8, that the colour and magnitude of the [O II] emitters correlate in the sense that brighter emitters in K tend to be redder in $z' - K$. Furthermore, in this cluster, the colour–magnitude diagram shows a deficit of red sequence galaxies with K fainter than ∼21.5 (Hayashi et al. 2010). Galaxy properties are thus strongly magnitude dependent. We therefore investigate the dependence of the fraction of red [O II] emitters on the K-band luminosity. It is found that the higher fraction of red [O II] emitters towards high density regions is dominated by massive [O II] emitters with $K < 21.5$ (Fig. 9). For less massive [O II] emitters with $K > 21.5$, the fraction of red [O II] emitters is very small, and is not strongly dependent on the environment. It is likely that massive [O II] emitters in high density regions change to red colours earlier than less massive ones and/or in lower density environments. This is consistent with the down-sizing scenario that more massive galaxies become quiescent galaxies earlier, and its environmental dependence in the sense that galaxy evolution (and down-sizing) proceeds earlier in higher density regions (e.g., Tanaka et al. 2005).

Fig. 10 shows the $J-K$ vs. $z'-K$ colour–colour diagram for the $6' \times 6'$ region in the cluster centre where J-band photometry is available. We utilize this diagram to investigate the nature of the red [O II] emitters. This method is analogous to the one that is used to separate between starburst galaxies and passive galaxies for Extremely Red Objects (EROs) based on the strength of the Balmer/4000Å break feature (e.g., Pozzetti & Mannucci 2000). In the XCS2215 cluster, Hilton et al. (2010) found eight 24μm sources with Spitzer/MIPS and three AGNs identified by Chandra X-ray data and Spitzer/IRAC mid-IR colours. Among them, we cross-identified seven dusty starbursts and three AGNs in our catalogue of cluster member candidates, and plot them together in the figure. The arrow shows a reddening vector estimated from the extinction curve of Calzetti et al. (2000). We can notice two sequences of galaxies on this diagram separated by the dashed line which is drawn in parallel to the reddening vector. One is for passively evolving galaxies with a redder $z' - K$ colour for a given $J - K$, and the other is star-forming galaxies which are distributed in the direction of the dust reddening vector extended from the blue-cloud. The three confirmed AGNs are distributed along the redder sequence for passive galaxies. Interestingly, none of the red

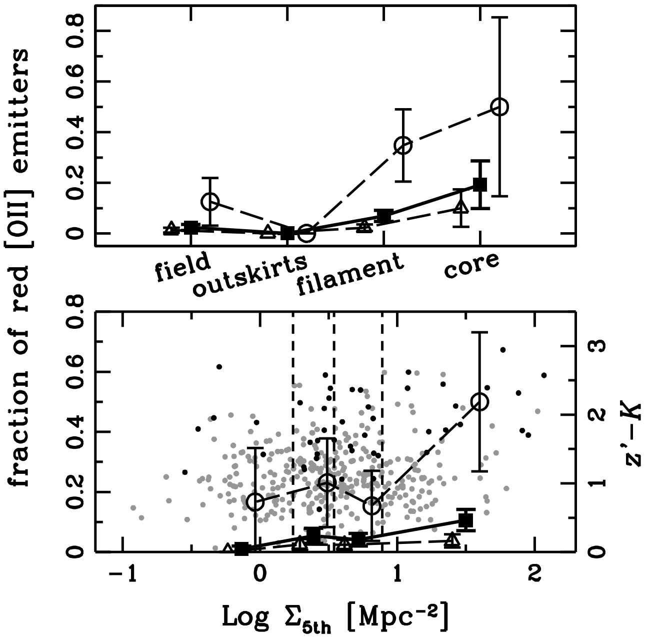

Figure 9. Fraction of the red [O II] emitters with $z' - K > 2.2$ to all the [O II] emitters is shown by the filled squares as a function of environment. Open circles and open triangles, connected by the long-dashed lines, show the fractions separated into bright and faint sample at $K = 21.5$, respectively. The data points are slightly offset manually to avoid their overlapping. The four environmental bins defined in §5.1 are used in the upper panel, while the local densities are used in the lower panel. In the lower panel, the black dots show the [O II] emitters with $K < 21.5$ and the gray dots show those with $K > 21.5$. Four density bins are separated by the vertical dashed lines. The right vertical axis shows $z' - K$ colours of the [O II] emitters.

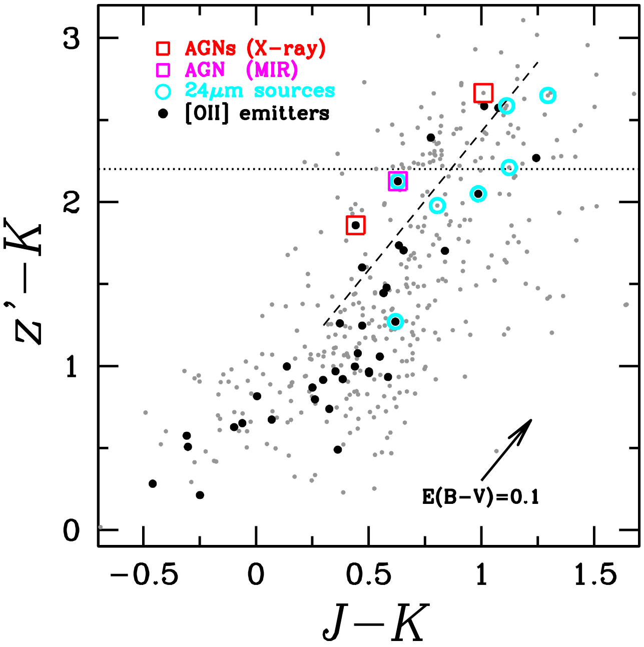

Figure 10. The colour–colour diagram of $J - K$ vs. $z' - K$ for the galaxies in the cluster centre where J-band photometry is available. Black dots show the [O II] emitters, and gray dots are the galaxies which meet our $Bz'K$ criteria given by the equation (1). Red and magenta squares show AGNs identified by X-ray and mid-infrared colours, respectively (Hilton et al. 2010). Cyan circles show dusty starburst galaxies which are detected in 24µm by Spitzer/MIPS (Hilton et al. 2010). The arrow shows a reddening vector corresponding to $E(B - V) = 0.1$, which is estimated from the extinction curve of Calzetti et al. (2000). The dashed line drawn in parallel to the reddening vector approximately separates between passive galaxies (upper) and dusty galaxies (lower). The dotted line shows the colour of $z' - K = 2.2$.

[O II] emitters are detected in 24µm, and most of them are located along the passive sequence with confirmed AGNs. Therefore, it is likely that a high fraction of red [O II] emitters in massive galaxies in the cluster core is caused by enhanced AGN activity in almost passively evolving galaxies.

Yan et al. (2006) found that [O II] emission lines from red galaxies tend to be produced by AGN activities rather than star forming activities in the local Universe. Lemaux et al. (2010) also found similar results at z=0.8–0.9. These support our results. The high fraction of red [O II] emitters in high density regions may suggest that AGN feedback is contributing to quench star formation activities in galaxies. In fact, as we discuss in §7.1, the line ratio diagnosis indicates a moderate level of AGN contribution in the [O II] emitters located in the central region of the XCS2215 cluster.

5.3 SFR, specific SFR, and stellar mass

In this section, we derive SFRs and specific SFRs (SSFRs) of the [O II] emitters from their [O II] line fluxes (ergs s^{-1} cm^{-2}) and continuum flux densities (ergs s^{-1} cm^{-2} $\mathrm{\AA}^{-1}$). They are calculated from flux densities in NB912 and z' bands (f_{NB912} and $f_{z'}$), respectively, as follows;

$$F([\mathrm{O\,II}]) = f_{NB912}\Delta_{NB912}\frac{1-(f_{z'}/f_{NB912})}{1-(\Delta_{NB912}/\Delta_{z'})}, \qquad (2)$$

$$f_{\lambda,\mathrm{cont}} = f_{z'}\frac{1-(f_{NB912}/f_{z'})(\Delta_{NB912}/\Delta_{z'})}{1-(\Delta_{NB912}/\Delta_{z'})}, \qquad (3)$$

where Δ_{NB912} and $\Delta_{z'}$ indicate FWHMs of the filters, and $\Delta_{NB912} = 134\mathrm{\AA}$ and $\Delta_{z'} = 955\mathrm{\AA}$.

The SFR is the fundamental quantity to characterize the star formation activity in a galaxy. We convert a [O II] luminosity into a SFR using the calibration by Kennicutt (1998). For a dust extinction correction, we take the following empirical approach. Garn et al. (2010) have found a correlation between the observed H α luminosity and the dust attenuation for H α emitters at $z = 0.845$ under the High-z Emission Line Survey (HiZELS) (equation (6) in Garn et al. 2010);

$$A_{\mathrm{H}\alpha} = -19.46 + 0.50\log_{10}\left(\frac{L_{\mathrm{H}\alpha,\mathrm{obs}}}{\mathrm{erg\ s^{-1}}}\right). \qquad (4)$$

Because the observed luminosity ratio between [O II] and H α is sensitive to dust extinction, the assumption of the constant $L_{[\mathrm{OII}]}/L_{\mathrm{H}\alpha}$ is inadequate. Moustakas et al. (2006) have found that the correlation between the observed ratio of [O II] to H α and $E(B-V)$ is consistent with the Galactic extinction curve of O'Donnell (1994) for local star-forming galaxies, and we get;

$$\log_{10}\left(L_{[\mathrm{OII}]}/L_{\mathrm{H}\alpha}\right)_{\mathrm{obs}} = -0.861\ E(B-V), \qquad (5)$$

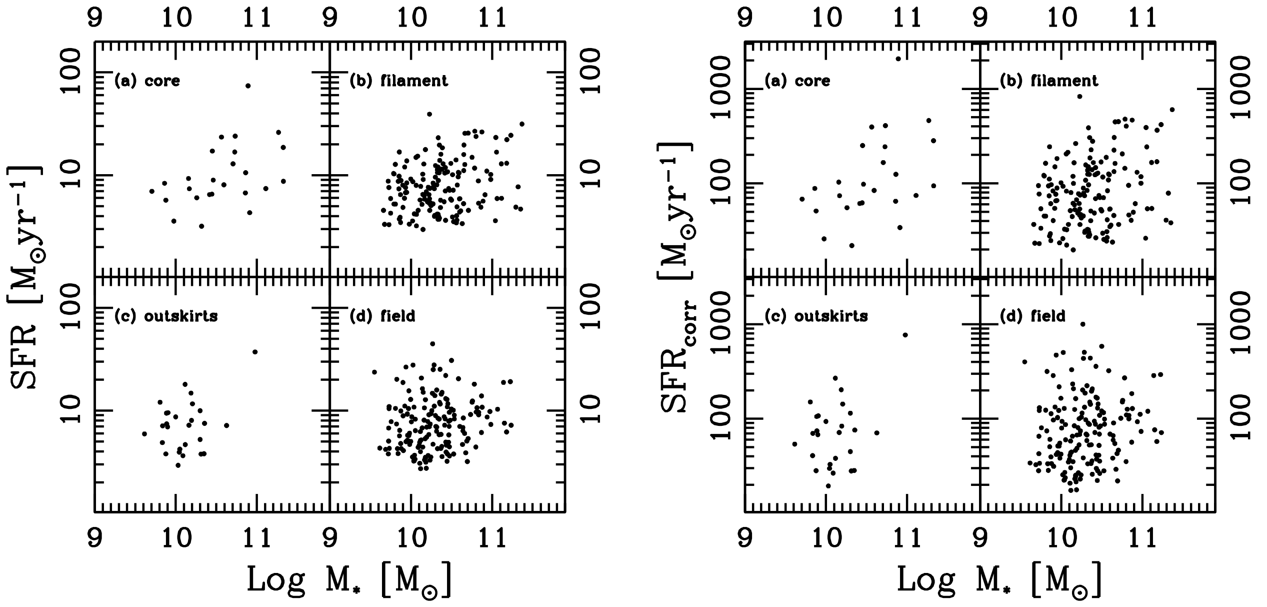

Figure 11. SFRs of the [O II] emitters as a function of stellar mass in four environments; (a) core, (b) filament, (c) outskirts, and (d) field. The left panel shows the SFRs converted from the observed [O II] luminosities, while the right panel shows the dust-corrected SFRs. See text for the details of the dust correction.

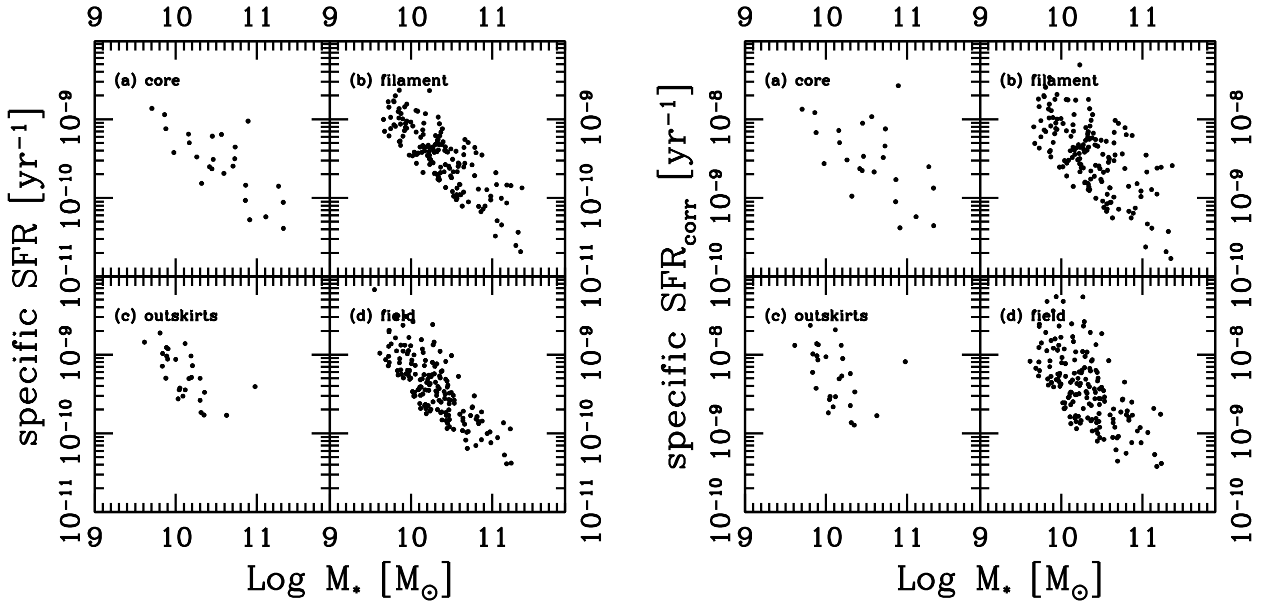

Figure 12. Same as Fig. 11, but for the specific SFRs.

$$= \quad -0.342\ A_{\mathrm{H}\alpha}, \qquad (6)$$

where $A_{\mathrm{H}\alpha} = 2.52E(B-V)$ assuming the Galactic extinction curve of O'Donnell (1994). Under the assumption that the two relations of (4) and (6) are valid for the [O II] emitters at $z = 1.46$, we use them to derive a H α luminosity, $L_{\mathrm{H}\alpha,\mathrm{obs}}$, and a dust attenuation index, $A_{\mathrm{H}\alpha}$, from the observed [O II] luminosity. Then, the dust-corrected H α luminosity is converted into a SFR$_{\mathrm{corr}}$ using the relation of Kennicutt (1998). It should be noted that the amounts of dust attenuation are comparable to those derived from the Balmer decrement of H β/H α (§ 7.2). Furthermore, we find that $E(B-V)$s derived from broad-band colours in $B-z'$ using the equation (4) of Daddi et al. (2004) are consistent with those derived from [O II] luminosities under the assumption that the ratio between stellar and nebulous components in dust extinction is 0.44 (Calzetti et al. 2000), although the

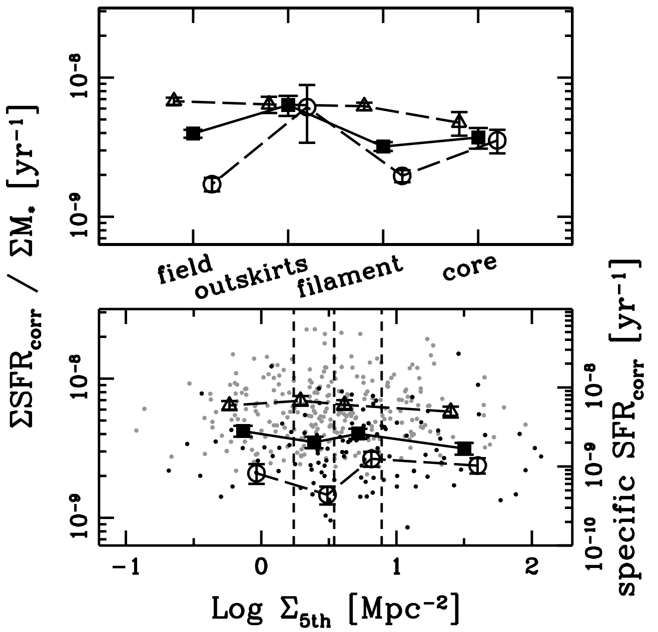

Figure 13. The integrated SSFR (ΣSFR/ΣM$_\star$) as a function of environment. The integrated SSFR is defined as the integrated SFR (ΣSFR) divided by the integrated stellar mass (ΣM$_\star$) for the [O II] emitters in each region. Filled squares show the integrated SSFRs for all the [O II] emitters. Open circles show those of [O II] emitters with M$_\star$> $10^{10.5}$M$_\odot$, while open triangles show those of the [O II] emitters with M$_\star$< $10^{10.5}$M$_\odot$. The data points are slightly offset manually to avoid their overlapping. In the lower panel, black dots show the SSFRs of the individual [O II] emitters with M$_\star$> $10^{10.5}$M$_\odot$, and gray dots are those of the [O II] emitters with M$_\star$< $10^{10.5}$M$_\odot$. The right vertical axis shows specific SFR.

scatter is large. These facts support that our dust correction method is valid.

For the [O II] emitters at $z = 1.46$, K-band corresponds to the rest-frame z'-band, i.e. ~8900Å. We estimate stellar masses of the [O II] emitters using an empirical relation between stellar mass for K-selected galaxies at $z > 1.4$ and its K magnitude given in Daddi et al. (2004). The mass-to-light ratio of a galaxy is calibrated with its $z - K$ colour, which can reduce the dispersion of derived stellar mass to $\sigma(\Delta \log(\mathrm{M}_\star)) = 0.20$ (Daddi et al. 2004). Using thus derived stellar mass of individual galaxies, we also derive SSFR by dividing SFR by the stellar mass.

Fig. 11 shows SFRs of the [O II] emitters in each environment as a function of stellar mass. There is a weak correlation that more massive galaxies tend to have larger SFRs, except for the [O II] emitters in the field region. It is also notable that, although there is a considerable scatter, for a given stellar mass, the [O II] emitters in the cluster have similar SFR$_{\rm corr}$ to those of field galaxies at $z = 1.5-2.5$ (Erb et al. 2006; Daddi et al. 2007; Hayashi et al. 2009; Yoshikawa et al. 2010). This suggests that, at $z = 1.46$ the environmental dependence of star formation activity is weak, and that galaxies in the XCS2215 cluster at $z = 1.46$ have conducted strong star formation activities just comparable to those in the general field.

Fig. 12 shows SSFR as a function of stellar mass, which suggests that more massive galaxies have lower SSFR. Massive galaxies do not necessarily enhance their star formation activity. We investigate the global SSFR, which are calculated from integrated SFR$_{\rm corr}$ divided by integrated stellar mass for the [O II] emitters in each environment (Fig. 13). This figure also supports that star formation activity of galaxies at $z = 1.46$ is not dependent on environment strongly.

At redshifts below unity or so, the star formation activity in clusters is significantly weaker than that in the surrounding regions. In RXJ1716.8+6708 cluster at $z = 0.81$ and XMMU J2235.3-2557 cluster at $z = 1.39$, no star-forming galaxies is found within ~200-250kpc from the cluster centre (Koyama et al. 2010; Lidman et al. 2008; Rosati et al. 2009; Bauer et al. 2011). However, Hayashi et al. (2010) and Hilton et al. (2010) found that there are a significant fraction of star-forming galaxies near the centre of the XCS2215 cluster. Fassbender et al. (2011) also found an on-going starburst activity in XMMU J1007.4+1237 cluster at $z = 1.56$. Most of the clusters at $z \gtrsim 1.5$ are likely to hold active star formation in the core regions. In order to make an evolutionary link to the lower-redshift clusters with inactive cores, some processes must take place to suppress star formation in the central regions in the short time interval between $z \sim 1.5$ and $z \sim 1.0$ ($\lesssim$ 1.5 Gyrs).

6 COSMIC EVOLUTION OF STAR FORMATION ACTIVITY IN CLUSTERS

In this section, we compare the global SSFR of the XCS2215 cluster with those of clusters at lower redshifts. For clusters at $z < 1$, the redshift evolution of the global SSFRs approximately follow a relation of $\sim (1+z)^6$ although the scatter is large (e.g., Finn et al. 2005; Koyama et al. 2010). For comparison with those previous studies, we derive integrated SSFR and dynamical mass of the XCS2215 cluster in the same manner as in the previous works.

To derive the integrated SFR (ΣSFR) in the XCS2215 cluster, we sum up individual SFR$_{\rm corr}$ of the [O II] emitters within a radius of $0.5\times R_{200}$, where R_{200} is a radius within which the averaged matter density is 200 times larger than the critical density. Previous studies apply a constant dust extinction, $A_{\mathrm{H}\alpha}$=1, to derive intrinsic SFRs, which is different from our correction for dust extinction adopted in this paper. Thus, for this comparison only, we apply the same amount of correction, $A_{\mathrm{H}\alpha}$=1. The cluster mass, M_{cl}, is estimated from the velocity dispersion of the cluster, which is 720 km s^{-1} (Hilton et al. 2010). Then, we use equations (4) and (5) in Koyama et al. (2010) to derive R_{200} and M_{cl} for the XCS2215 cluster. The radius, R_{200}, is 0.8 Mpc which corresponds to 1.57 arcmin (Hilton et al. 2010). The mass, M_{cl}, is 2.81×10^{14}M$_\odot$. As a result, the integrated SFR, ΣSFR, is 764 ± 23.3M$_\odot$yr^{-1}.

Before comparing with the previous studies, there are two issues to keep in mind. One is that R_{200} and M_{cl} derived from the velocity dispersion may be overestimated. Hilton et al. (2010) pointed out that the redshift distribution of cluster members shows a bimodality, and thus this cluster may have been experiencing a merger event in the recent past within a few Gyr or so. Our spectroscopy also shows a similar redshift distribution for the [O II] emitters. The other issue is that our [O II] survey may be underestimating the

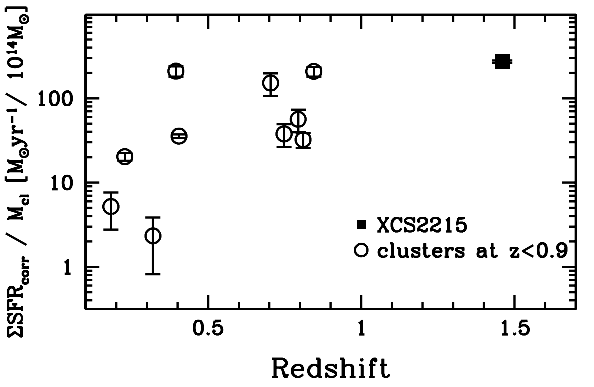

Figure 14. The integrated SFR per unit cluster mass ($\Sigma\mathrm{SFR}_{\mathrm{corr}}/M_{\mathrm{cl}}$) is plotted as a function of redshift. The integrated SFR, $\Sigma\mathrm{SFR}_{\mathrm{corr}}$, is a sum of the SFR corrected for dust extinction assuming $A_{\mathrm{H}\alpha} = 1$. The cluster mass, M_{cl}, is derived from the velocity dispersion. The filled square shows our data point of the XCS2215 cluster. Open circles show other clusters taken from the literature; A1689 ($z = 0.183$) from Balogh et al. (2002), A2390 ($z = 0.228$) from Balogh & Morris (2000), AC114 ($z = 0.320$) from Couch et al. (2001), CL0024.0+1652 ($z = 0.395$) from Kodama et al. (2004), A851 ($z = 0.41$) from Koyama et al. (2011), CL1040 ($z = 0.704$), CL1054-12 ($z = 0.748$) and CL1216 ($z = 0.794$) from Finn et al. (2005), RXJ1716($z = 0.81$) from Koyama et al. (2010), and CLJ0023+0423B ($z = 0.845$) from Finn et al. (2004).

integrated SFR compared to the H α surveys. Our SSFRs are derived from [O II] luminosities, while the SSFRs in the other studies are derived from H α luminosities. Our [O II] survey is probably more sensitive to dust extinction and the depth (2.6M$_\odot$yr^{-1}) is also slightly shallower than the H α surveys (<1M$_\odot$yr^{-1}) at lower redshifts in terms of dust-free limiting star formation rates. In spite of such differences between our study and the previous ones, however, it is still worth comparing among these results.

Fig. 14 shows the SSFRs of clusters as a function of redshift. The XCS2215 cluster has the largest SSFR among the clusters plotted in the figure, and there is a general trend that the star formation activity in galaxy clusters increases with redshift out to $z \sim 1.46$. It should be noted that both of the two issues described above lead to the conservative estimation of SSFR for the XCS2215, which would therefore strengthen the trend that we claim. This result seems reasonable, because the cosmic star formation rate density keeps rising to $z \sim 2$ on average and the redshift of $z = 1.46$ is closer to the epoch when galaxy clusters are formed. Tadaki et al. (2011) suggest that the star formation activity in cluster/proto-cluster may be even stronger than in the field at $z \sim 2$. As suggested in § 5, the redshift range of z =1.5–2.5 is probably the epoch when galaxies form stars very actively irrespective of their environments.

7 SPECTROSCOPIC PROPERTIES OF THE [O II] EMITTERS

In this section, we discuss spectroscopic properties of the [O II] emitters using the ratios of detected emission lines. Table 4 shows the observed [O II] luminosities and the ratios of emission lines.

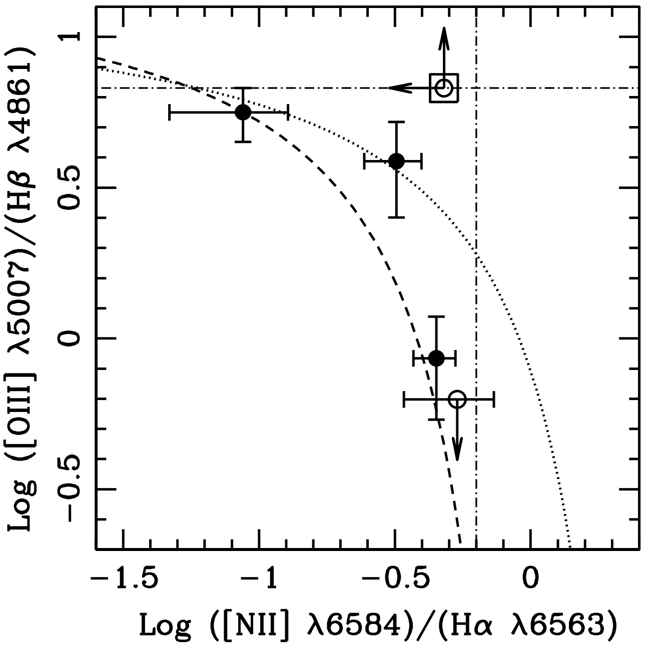

Figure 15. The emission-line diagnostic diagram showing [O III](λ5007)/H β vs. [N II](λ6584)/H α ratios. The dashed curve shows the boundary separating star forming galaxies and AGNs based on the SDSS data (Kauffmann et al. 2003). The dotted curve shows a theoretical boundary given in Kewley et al. (2001). Star forming galaxies are located on the bottom/left side of the curves, while AGNs are located on the top/right side. The region between the two curves is a composite region, where both star formation and AGN are contributing. Filled circles show the [O II] emitters with all the lines detected, while open circles indicate those with some lines un-detected and 2σ sky noise levels are shown as upper/lower limits. The definitive AGN is marked by an open square. The dot-dashed lines show Log([N II](λ6584)/H α)=-0.2 and Log([O III](λ5007)/H β)=0.83, which are used to separate AGNs when only either of the ratios can be measured (Fig. 16).

7.1 AGN contribution

Since the AGN activity in the Universe peaks at $z \sim 2$ (e.g., Ueda et al. 2003), it is important to investigate a contribution of AGN to our [O II] emitters before discussing their spectroscopic properties. Yan et al. (2006) investigated the origin of [O II] emission lines from local galaxies using the SDSS data, and concluded that [O II] emission lines from red galaxies are dominated by radiation from low-ionization nuclear emission-line regions (LINERS), rather than star-forming HII regions. On the other hand, [O II] emission lines from blue galaxies mainly come from star formation. Lemaux et al. (2010) conducted NIR spectroscopy of LINER-type galaxies in clusters at z=0.8–0.9 and obtained similar conclusions to those of Yan et al. (2006). Although most of our [O II] emitters have blue colours hence their [O II] emissions are likely due to star formation, these studies demonstrate the importance of evaluating the AGN contribution in our [O II] emitters.

The two emission line ratios of [N II]/H α and [O III]/H β are frequently utilized to distinguish star-forming galaxies from AGNs (e.g., Baldwin et al. 1981; Kewley et al. 2001; Kauffmann et al. 2003). Fig. 15 shows a [N II]/H α vs. [O III]/H β diagram for our [O II] emitters in the XCS2215

Table 4. Line properties of our 16 spectroscopically confirmed [O II] emitters. The observed [O II] luminosities, ratios of emission lines, color excesses, and oxygen abundances are shown.

ID	[O II] flux^{†,a}	[O II] luminosity^{†,b}	H α/H β	$E(B-V)^c$	[N II]/H α	Z(N2)^d	[O III]/H β	Z(O3H β)^e	Comment
1	0.58±0.08	0.77±0.11	—	—	0.29±0.10	$8.59^{+0.07}_{-0.11}$	—	—	—
2	3.90±0.14	5.15±0.19	—	—	—	—	>21.40	—	AGN
3	0.54±0.13	0.73±0.17	—	—	<0.28	<8.582	—	—	—
4	1.17±0.09	1.56±0.12	—	—	—	—	2.80±1.26	$8.46^{+0.21}_{-0.18}$	—
5	0.41±0.09	0.55±0.12	—	—	0.34±0.23	$8.63^{+0.13}_{-0.28}$	—	—	—
6	0.72±0.10	0.93±0.13	—	—	<0.48	—	>6.77	—	AGN
7	1.33±0.13	1.75±0.18	5.06±1.57	$0.54^{+0.36}_{-0.26}$	0.54±0.20	$8.75^{+0.08}_{-0.11}$	<0.63	>8.899	—
8	2.30±0.13	3.06±0.17	7.44±2.54	$0.91^{+0.40}_{-0.28}$	0.32±0.08	$8.62^{+0.05}_{-0.07}$	3.87±1.35	$8.31^{+0.20}_{-0.24}$	—
9	1.64±0.12	2.20±0.16	—	—	—	—	>7.94	—	AGN
10	1.27±0.09	1.67±0.12	4.36±0.81	$0.40^{+0.20}_{-0.16}$	0.45±0.08	$8.70^{+0.04}_{-0.05}$	0.86±0.32	$8.83^{+0.11}_{-0.08}$	—
11	0.98±0.11	1.31±0.15	—	—	—	—	>2.19	<8.555	—
12	0.94±0.12	1.27±0.17	—	—	—	—	2.02±0.58	$8.58^{+0.11}_{-0.09}$	—
13	0.23±0.07	0.29±0.09	—	—	—	—	<0.86	>8.824	—
14	0.29±0.10	0.40±0.13	—	—	—	—	>3.15	<8.412	—
15	1.04±0.09	1.39±0.12	5.97±1.33	$0.70^{+0.24}_{-0.19}$	0.09±0.04	$8.30^{+0.09}_{-0.15}$	5.63±1.14	$7.87^{+0.35}_{-0.35}$	—
16	0.38±0.08	0.51±0.11	—	—	—	—	>3.10	<8.419	—

† Corrected for the filter response based on the spectroscopic redshift.
a The numbers are in the units of 10^{-16} erg s^{-1} cm^{-2}.
b The numbers are in the units of 10^{42} erg s^{-1}.
c $E(B-V)$ is derived from the Balmer decrement (H α/H β ratio).
d Z(N2) is oxygen abundance, 12+log(O/H), estimated from the [N II]/H α ratio.
e Z(O3H β) is oxygen abundance, 12+log(O/H), estimated from the [O III]/H β ratio.

cluster. The dashed line shows a boundary separating between star forming galaxies and AGNs, which is defined based on the SDSS data (Kauffmann et al. 2003). The dotted line shows a theoretical boundary given by Kewley et al. (2001). For our spectroscopic sample, there are only three [O II] emitters with all the emission lines detected (see Table 3). If either of the line ratios is not available, we evaluate an upper or lower limit of the ratio by assuming a Gaussian profile with a peak flux that is twice the sky noise and $\sigma = 10$Å for the non-detected line. We note that the assumed width of the Gaussian profile is comparable to those of the detected lines. We show the galaxies with such upper/lower limit(s) by open circles with arrow(s) in Fig. 15. Fig. 16 shows [N II]/H α and [O III]/H β ratios, separately. The number of objects shown in the plots is significantly increased. The dot-dashed lines indicate Log([N II]/H α)$= -0.20$ and Log([O III]/H β)$= 0.83$, respectively, above which emission line ratios are more AGN-like.

Almost all the [O II] emitters for which all the four emission lines are available are located in the composite region between the dotted and the broken lines in Fig. 15. Only one of them is clearly in the AGN region. Fig. 16 also shows that few [O II] emitters have a large contribution of AGN. Only three [O II] emitters are located above the threshold lines for AGN. Therefore, it is unlikely that our [O II] emitters are dominated by AGNs. Although the red [O II] emitters may have more contribution of LINER/Seyfert-type AGNs as pointed out by the previous studies (Yan et al. 2006; Lemaux et al. 2010), Fig. 8 shows that a large fraction of our [O II] emitters are distributed in the blue cloud, and thus most of the [O II] emission lines are more likely to be originating from star formation activity rather than AGN. At the same time, however, AGN contribution is not negligible, and a part of the [O II] emission line fluxes may come from AGNs.

Hilton et al. (2010) detected two X-ray point sources with Chandra among the spectroscopically confirmed members of XCS2215 cluster, whose limiting fluxes are $\approx 1.0 \times 10^{-16}$ erg s^{-1} cm^{-2} corresponding to $L_{\rm X(2-10keV)} \gtrsim 0.8 \times 10^{42}$ erg s^{-1} at $z = 1.46$ if the spectral index of $\alpha = 2$ and $N_{\rm H} = 1.0 \times 10^{22}$ cm^{-2} are assumed (Hilton et al. 2010). Moreover, they found that one of the 24μm sources has a mid-infrared SED based on the Spitzer data that is consistent with an AGN although none of the 24μm sources are detected in the X-ray data. Among these three AGN candidates, two of them (a X-ray source and a 24μm source) are included in our [O II] emitter sample. The X-ray source is ID-2 of the [O II] emitters, while no line is detected in our MOIRCS spectrum for the 24μm source. This suggests that most of our [O II] emitters are not heavily contaminated by AGN activities, except for the red [O II] emitters (§ 5.2 and Fig. 10).

All these results support that the XCS2215 cluster has active star forming activities even in the core of the cluster as reported in Hayashi et al. (2010) and Hilton et al. (2010). As Figs 15 and 16 indicate, we cannot completely ignore the contribution from AGNs, and in principle, we must take care of the influence of AGN on the line flux when we discuss the properties based on the emission line fluxes. However, since it is impossible to quantitatively measure a contribution of AGN to the line flux with the currently available data, we have to assume at this stage that [O II] fluxes originate purely from star formation in §5.3. It should be noted

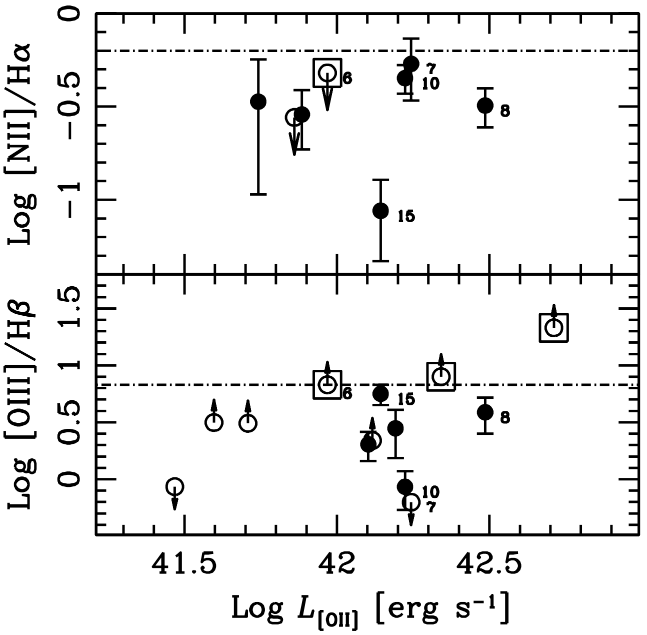

Figure 16. The emission-line ratios as a function of [O II] luminosity. The upper panel shows [N II](λ6584)/H α ratios, while the lower panel shows [O III](λ5007)/H β ratios. Filled circles indicate the objects with both of the lines detected. Open circles indicate those without either of the lines, and thus these line ratios are upper/lower limits. The dot-dashed lines show Log([N II](λ6584)/H α)=-0.2 and Log([O III](λ5007)/H β)=0.83. Three AGNs candidates are marked by open squares. The numbers indicated beside the symbols correspond to the ID numbers of the [O II] emitters as listed in Table 4 for comparison.

therefore that the SFRs derived from the [O II] luminosities are probably overestimated.

7.2 Dust extinction

The galaxy properties derived from the observables (colours and line intensities) are sensitive to the correction for dust extinction. In order to estimate the amount of dust extinction for stellar continuum flux, the SED fitting to the multi-band photometric data is frequently conducted. However, it is hard to break the degeneracy between stellar age and dust reddening. Also the amount of dust extinction for the nebular emission lines from HII regions is different from that of the stellar continuum SEDs. A large uncertainty exists in the conversion from stellar reddening to nebular reddening.

One of the reliable methods to derive the amount of dust extinction of the nebular emission is to use the Balmer decrement (i.e. H α/H β ratio). Under the assumption of the Case B recombination, intrinsic flux ratio of the two Balmer lines is expected to $(\mathrm{H}\,\alpha/\mathrm{H}\,\beta)_{\mathrm{int}} = 2.86$. By comparing the observed flux ratio, $(\mathrm{H}\,\alpha/\mathrm{H}\,\beta)_{\mathrm{obs}}$, with the intrinsic one, we can estimate the amount of dust extinction as follows;

$$E(B-V) = -\frac{2.5}{k(\lambda_{H\beta}) - k(\lambda_{H\alpha})} \log\left\{\frac{(H\alpha/H\beta)_{\mathrm{int}}}{(H\alpha/H\beta)_{\mathrm{obs}}}\right\}, \quad (7)$$

where $k(\lambda_{H\beta}) - k(\lambda_{H\alpha}) = 1.14$ as calculated from the O'Donnell (1994) extinction curve (as in §5.3).

There are four [O II] emitters in our spectroscopic sample for which both of the Balmer lines are detected. The derived amounts of dust extinction are $E(B-V) = 0.543^{+0.355}_{-0.258}$, $0.910^{+0.397}_{-0.279}$, $0.401^{+0.197}_{-0.163}$, and $0.700^{+0.240}_{-0.192}$ for ID-7, ID-8, ID-10 and ID-15, respectively. These colour excesses correspond to $A_{\mathrm{H}\alpha}$= $1.37^{+0.89}_{-0.65}$, $2.29^{+1.00}_{-0.70}$, $1.01^{+0.50}_{-0.41}$, and $1.76^{+0.60}_{-0.48}$, respectively. Note that these $E(B-V)$ values are comparable to those of the BzK-selected field galaxies (Yoshikawa et al. 2010). The estimated dust extinction is larger than the nominal value of H α flux, $A_{\mathrm{H}\alpha}$=1 that is frequently used in the literature. If we correct [O II] fluxes only by the amount corresponding to $A_{\mathrm{H}\alpha}$=1 for all our emitters uniformly, the intrinsic [O II] fluxes are likely to be underestimated significantly.

For the two [O II] emitters of ID-6 and ID-8, both [O II] and H α lines are detected. The observed ratio of the two lines can provide us with another estimation of $A_{\mathrm{H}\alpha}$ using the equation (6). The observed ratios, $L_{[\mathrm{OII}]}/L_{\mathrm{H}\alpha}$, for ID-6 and ID-8 [O II] emitters are 0.393±0.217 and 0.438±0.066, respectively. These correspond to $A_{\mathrm{H}\alpha}$=$1.19^{+1.02}_{-0.56}$ and $1.05^{+0.21}_{-0.18}$, respectively. For the ID-8, two independent measures of dust attenuation differ by a large amount (∼1 mag) although the uncertainties of the both measurements are large. Such discrepancy may be caused by a contribution of an AGN to the line fluxes.

In §5, we use the dust extinction law which is dependent on SFR (i.e., H α luminosity). Here, we can verify whether the Garn et al. (2010) relation is valid for our [O II] emitters using the spectroscopic sample. In the same manner as in §5, we estimate $A_{\mathrm{H}\alpha}$ from the [O II] flux derived from the narrow-band imaging but is corrected for filter response using the accurate spectroscopic redshift. We obtain $A_{\mathrm{H}\alpha}$=1.9–2.1 based on the Garn et al. (2010) relation, which is consistent with the estimated value by the Balmer decrement technique. Therefore our method of dust extinction correction based on the Garn et al. (2010) relation is confirmed to be valid for the [O II] emitters (§5). However, it is possible that [O II] fluxes are slightly over-corrected for dust extinction, and thus $\mathrm{SFR}_{\mathrm{corr}}$ for the [O II] emitters may be a little overestimated.

7.3 Gas-phase metallicity

It is well known that the electron temperature reflects gas metallicity (Kewley & Dopita 2002; Kobulnicky & Kewley 2004; Erb et al. 2006). Because the auroral lines which are used to derive electron temperature are weak and can be observed only for galaxies with low metallicities, it is very difficult to estimate gaseous metallicity even for the local galaxies with this method. We can only use the ratios of strong emission lines which are emitted from different ionization levels, to derive gaseous metallicities of high-z galaxies. There are several metallicity diagnostics that have been invented, namely R_{23} and N2 methods which can estimate gas-phase oxygen abundance, 12+log(O/H). However, different methods do not always give consistent oxygen abundances. Even if the same diagnostic is used, different calibrations lead to very different metallicities (Kewley & Dopita 2002; Kobulnicky & Kewley 2004). Therefore, one should make sure to use the same diagnostics and calibration in order to make any proper comparison with other results.

We derive gas phase metallicities of our [O II] emitters using the two diagnostics. One is based on H α/[N II] flux

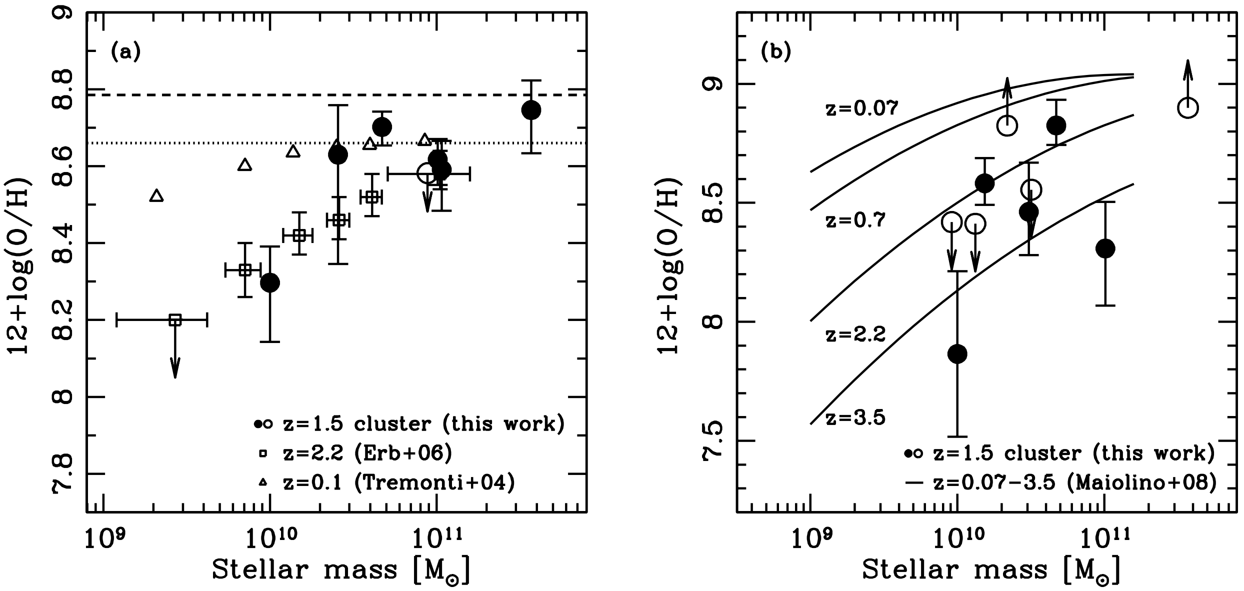

Figure 17. (a) Left panel: mass–metallicity relation for the [O II] emitters in the XCS2215 cluster. Metallicities are derived from [N II]/Hα line ratios. Filled circles show the objects with both of the lines detected, while open circles show those with only either of the lines detected. Arrows indicate upper/lower limits in metallicity. Open squares show UV-selected galaxies at $z \sim 2$, and open triangles indicate the local star-forming galaxies (Tremonti et al. 2004; Erb et al. 2006). The dotted line corresponds to the solar oxygen abundance of 12+log(O/H) = 8.66 (Asplund et al. 2004). The dashed line shows the abundance for galaxies with the flux ratio of log([N II]/Hα)=-0.2. Objects with [N II]/Hα ratio larger than the value are likely to be an AGN (§7.1). (b) Right panel: same as the left panel, but for metallicities derived from [O III]/Hβ line ratios. Solid lines show mass–metallicity relations at z =0.07, 0.7, 2.2, and 3.5 (Maiolino et al. 2008).

ratios and its calibration by Pettini & Pagel (2004), and the other is based on Hβ/[O III] flux ratios and its calibration by Maiolino et al. (2008). Both diagnostics are not sensitive to dust extinction, because the wavelength difference of the pair lines is very small. If only either of the lines is detected, the upper/lower limit of metallicity is estimated. Fig. 17 shows thus derived metallicities of our [O II] emitters in the XCS2215 cluster plotted as a function of stellar mass. Fig. 17(a) shows the metallicities from Hα/[N II] ratios, while Fig. 17(b) shows the metallicities from Hβ/[O III] ratios. Stellar masses are already derived in §5. In both panels, we also show the mass–metallicity relations at different redshifts taken from the literature (Tremonti et al. 2004; Erb et al. 2006; Maiolino et al. 2008) for comparison.

Although the error bars are large, Fig. 17 suggests that there is a weak mass–metallicity relation in the sense that more massive galaxies have higher metallicities. The metallicities of our [O II] emitters are comparable to those of the galaxies at z=2–3 (Erb et al. 2006; Maiolino et al. 2008). Our sample has the galaxies in a high density galaxy cluster, while the samples of the above previous studies are the galaxies in the general field at z=2–3. It seems that the star-forming galaxies in the cluster at $z = 1.46$ have a similar mass–metallicity relation to that of the field galaxies at z=2–3. Although the redshift range is slightly different, this may suggest that the mass–metallicity relation is not very dependent on environment at $z \gtrsim 1.5$. Here, we must take into account the contribution of AGN to the line flux ratios. A larger contribution of AGN would make both [N II]/Hα and [O III]/Hβ larger, meaning that the derived metallicities are over-estimated with [N II]/Hα and under-estimated with [O III]/Hβ, respectively. As discussed in the previous section, our [O II] emitters may have a moderate level of AGN contribution. In fact, the metallicities estimated by the two different line ratios are not in good agreement. However, we can still trust the relative trend such as the existence of the mass-metallicity relation (but not its absolute values) as far as the same method is used uniformly. In order to quantify the evolution of the mass–metallicity relation at $z \gtrsim 1.5$, we need to evaluate the AGN contribution, but it is beyond the scope of this paper.

The fact that the mass–metallicity relation for the XCS2215 cluster is similar to that of the field at $z \sim 2$, may further support the lack of environmental dependence, due probably to the high star formation activity in the cluster cores at this high redshift comparable to that in the field.

8 SUMMARY

We conduct a wide-field survey of [O II] emission line galaxies in and around the XMMXCS J2215.9-1738 cluster at $z = 1.46$ with Subaru/Suprime-Cam. This survey is an extension of our previous study reported in Hayashi et al. (2010) which was limited to the central $6' \times 6'$ region of the cluster. By combining the UKIRT K imaging data, we have now extended the analyses to the entire $32' \times 23'$ region. We investigate colours and star formation activities of the [O II] emitters in various environments from the cluster core to the surrounding field at $z = 1.46$. Moreover, we conduct a follow-up near-infrared spectroscopy of 34 [O II] emitters in the cluster core identified in Hayashi et al. (2010) with Subaru/MOIRCS, and obtain zJ spectra covering a wavelength range of 0.9–1.8μm. These spectra enable us to confirm the existence of [O II] emission lines, and to investigate the detailed properties of the [O II] emitters on the basis of multiple nebular emission lines such as Hβ, [O III], Hα, and [N II]. Our findings are summarized below.

(i) We select 380 [O II] emitters at $z = 1.46$ down to a line flux of 1.4×10^{-17} erg s^{-1} cm^{-2} in our entire survey area of $32' \times 23'$. The spatial distribution of the [O II] emitters shows a well-defined filamentary structure of star forming galaxies to the east/south of the cluster as well as a concentration of such galaxies in the cluster core. The filament is one of the largest structures of star-forming galaxies at high redshifts ($1.3 \lesssim z \lesssim 3$). Based on the 2D structures, we define four different environments, namely, cluster core, outskirts, filament, and the field, in order to investigate the environmental dependence of the properties of star-forming galaxies at $z = 1.46$.

(ii) We spectroscopically confirm that at least 16 [O II] emitters are certainly located at $z = 1.46$ out of 34 targeted [O II] emitter candidates in the cluster core. Only a single emission line is detected at ∼9100Å for three candidates. The other 15 candidates have no detected emission lines. However, the [O II] fluxes estimated by the narrowband imaging suggest that it is likely that most of them have fluxes of emission lines smaller than the limiting flux. This thus assures that our photometric selection technique is valid to efficiently sample [O II] emitters at $z = 1.46$. The redshift distribution of the confirmed emitters is consistent with that of the confirmed cluster members reported in Hilton et al. (2010), and is likely to have a double-peak feature.

(iii) The $z' - K$ vs. K colour–magnitude diagram shows a higher fraction of [O II] emitters on the red sequence in the cluster region than that in the other environments. This suggests that some processes which work in the cluster core are responsible for the red colours of some [O II] emitters. It is also noted that most of the red [O II] emitters are massive galaxies. Their SEDs indicate that they are more likely passive galaxies with AGNs. We argue therefore that AGN feedback may be a good candidate for physical processes to quench star formation activities in massive galaxies in high-density regions.

(iv) The cluster (XMMXCS J2215.9-1738) has been conducting star formation at rates comparable to those in other environments. This supports our previous study (Hayashi et al. 2010) which found a high star formation activities in the cluster central region. It is also found that the global specific star formation rate of galaxy cluster, which is calculated as the integrated SFRs divided by the integrated stellar masses of galaxies within a radius of $0.5 \times R_{200}$, increases with redshift up to $z = 1.46$.

(v) We investigate the flux ratios of emission lines, [O III]/Hβ and [N II]/Hα, to distinguish between star-forming galaxies and AGNs. On a diagram showing both line ratios, our [O II] emitters are preferentially located in the intermediate, composite region where both star-formation and AGN are likely to be contributing. It is therefore unlikely that many of the [O II] emitters are heavily contaminated by strong AGNs, but at the same time it is likely that the AGN contribution is not negligible.

(vi) We estimate the strength of dust extinction from the Balmer decrement measurements (Hβ/Hα) for four of the [O II] emitters where both lines are detected. It is found that the extinction index $E(B-V)$ ranges from 0.40 to 0.91, suggesting that [O II] emission line flux is considerably subject to dust extinction.

(vii) We derive gas-phase metallicities for the [O II] emitters from [N II]/Hα or [O III]/Hβ line ratios where available. It is found that our emitters in the cluster at $z = 1.46$ are located on a mass–metallicity relation, which is similar to that of the star-forming galaxies in the field at $z \sim 2$. This may also suggest that the star formation activity at $z \sim 1.5$ and beyond is not strongly dependent on environment.

In summary, we find that star formation activity of galaxies at $z = 1.46$ is not yet strongly dependent on environment, and that even the cluster core is experiencing high star forming activity comparable to those in other lower-density regions. Our results also suggest that more detailed understanding of AGN activities along with star formation activities is crucial to reveal galaxy evolution in clusters in particular the physical mechanisms of quenching star formation. Larger, systematic near-infrared spectroscopic surveys such as those capable with Subaru/FMOS will enable us to understand the inter-relationship between galaxy and AGN activities, and their co-evolution.

ACKNOWLEDGMENTS

Most of the imaging data and all of the spectroscopic data used in this paper are collected at Subaru Telescope, which is operated by the National Astronomical Observatory of Japan. We thank the Subaru Telescope staff for their invaluable help to assist our observations with Suprime-Cam and MOIRCS. A part of NIR data are collected at the UKIRT, which is operated by the Joint Astronomy Centre on behalf of the Science and Technology Facilities Council of the U.K. We also thank the UKIRT staff for their invaluable help to assist our observations with WFCAM. We thank Dr. Kentaro Motohara for kindly providing us with his data reduction package for UKIRT/WFCAM. We would like to thank an anonymous referee for carefully reading our manuscript and giving useful comments. Y.K. acknowledges support from the Japan Society for the Promotion of Science (JSPS) through JSPS Research Fellowship for Yong Scientists. T.K. acknowledges support in part by a Grant-in-Aid for the Scientific Research (No. 21340045) by the Japanese Ministry of Education, Culture, Sports, Science and Technology.

REFERENCES

Asplund M., Grevesse N., Sauval A. J., Allende Prieto C., Kiselman D., 2004, A&A, 417, 751
Baldwin J. A., Phillips M. M., Terlevich R., 1981, PASP, 93, 5
Balogh M. L., Couch W. J., Smail I., Bower R. G., Glazebrook K., 2002, MNRAS, 335, 10
Balogh M. L., Morris S. L., 2000, MNRAS, 318, 703

Bauer A. E., Grützbauch R., Jørgensen I., Varela J., Bergmann M., 2011, MNRAS, 411, 2009

Bertin E., Arnouts S., 1996, A&AS, 117, 393

Blakeslee J. P. et al., 2003, ApJL, 596, L143

Bohlin R. C., Gilliland R. L., 2004, AJ, 128, 3053

Bower R. G., Lucey J. R., Ellis R. S., 1992, MNRAS, 254, 601

Brammer G. B., van Dokkum P. G., Coppi P., 2008, ApJ, 686, 1503

Calzetti D., Armus L., Bohlin R. C., Kinney A. L., Koornneef J., Storchi-Bergmann T., 2000, ApJ, 533, 682

Cardelli J. A., Clayton G. C., Mathis J. S., 1989, ApJ, 345, 245

Casali M. et al., 2007, A&A, 467, 777

Coleman G. D., Wu C., Weedman D. W., 1980, ApJS, 43, 393

Couch W. J., Balogh M. L., Bower R. G., Smail I., Glazebrook K., Taylor M., 2001, ApJ, 549, 820

Daddi E., Cimatti A., Renzini A., Fontana A., Mignoli M., Pozzetti L., Tozzi P., Zamorani G., 2004, ApJ, 617, 746

Daddi E. et al., 2007, ApJ, 670, 156

De Lucia G. et al., 2007, MNRAS, 374, 809

Doherty M. et al., 2010, A&A, 509, A83

Erb D. K., Shapley A. E., Pettini M., Steidel C. C., Reddy N. A., Adelberger K. L., 2006, ApJ, 644, 813

Erb D. K., Steidel C. C., Shapley A. E., Pettini M., Reddy N. A., Adelberger K. L., 2006, ApJ, 647, 128

Fassbender R. et al., 2011, A&A, 527, L10

Finn R. A., Zaritsky D., McCarthy Jr. D. W., 2004, ApJ, 604, 141

Finn R. A. et al., 2005, ApJ, 630, 206

Garn T. et al., 2010, MNRAS, 402, 2017

Gobat R. et al., 2011, A&A, 526, 133

Gunn J. E., Stryker L. L., 1983, ApJS, 52, 121

Hayashi M., Kodama T., Koyama Y., Tanaka I., Shimasaku K., Okamura S., 2010, MNRAS, 402, 1980

Hayashi M. et al., 2009, ApJ, 691, 140

Henry J. P. et al., 2010, ApJ, 725, 615

Hilton M. et al., 2010, ApJ, 718, 133

Hilton M. et al., 2009, ApJ, 697, 436

Hopkins A. M., Beacom J. F., 2006, ApJ, 651, 142

Ichikawa T. et al.,2006, in Society of Photo-Optical Instrumentation Engineers (SPIE) Conference Series Vol. 6269 of Society of Photo-Optical Instrumentation Engineers (SPIE) Conference Series, MOIRCS: multi-object infrared camera and spectrograph for SUBARU

Kajisawa M., Kodama T., Tanaka I., Yamada T., Bower R., 2006, MNRAS, 371, 577

Kauffmann G. et al., 2003, MNRAS, 346, 1055

Kennicutt Jr. R. C., 1998, ARA&A, 36, 189

Kewley L. J., Dopita M. A., 2002, ApJS, 142, 35

Kewley L. J., Dopita M. A., Sutherland R. S., Heisler C. A., Trevena J., 2001, ApJ, 556, 121

Kobulnicky H. A., Kewley L. J., 2004, ApJ, 617, 240

Kodama T., Arimoto N., Barger A. J., Arag'on-Salamanca A., 1998, A&A, 334, 99

Kodama T., Balogh M. L., Smail I., Bower R. G., Nakata F., 2004, MNRAS, 354, 1103

Kodama T., Tanaka I., Kajisawa M., Kurk J., Venemans B., De Breuck C., Vernet J., Lidman C., 2007, MNRAS, 377, 1717

Kong X. et al., 2006, ApJ, 638, 72

Koyama Y., Kodama T., Nakata F., Shimasaku K., Okamura S., 2011, ApJ, in press, arXiv:1103.2180

Koyama Y., Kodama T., Shimasaku K., Hayashi M., Okamura S., Tanaka I., Tokoku C., 2010, MNRAS, 403, 1611

Koyama Y. et al., 2008, MNRAS, 391, 1758

Kriek M., van der Wel A., van Dokkum P. G., Franx M., Illingworth G. D., 2008, ApJ, 682, 896

Kurk J. et al., 2009, A&A, 504, 331

Landolt A. U., 1992, AJ, 104, 340

Lemaux B. C., Lubin L. M., Shapley A., Kocevski D., Gal R. R., Squires G. K., 2010, ApJ, 716, 970

Lidman C. et al., 2008, A&A, 489, 981

Ly C. et al., 2007, ApJ, 657, 738

Maiolino R. et al., 2008, A&A, 488, 463

Mannucci F., Cresci G., Maiolino R., Marconi A., Gnerucci A., 2010, MNRAS, 408, 2115

Mannucci F. et al., 2009, MNRAS, 398, 1915

Miyazaki S. et al., 2002, PASJ, 54, 833

Moustakas J., Kennicutt Jr. R. C., Tremonti C. A., 2006, ApJ, 642, 775

O'Donnell J. E., 1994, ApJ, 422, 158

Onodera M., Arimoto N., Daddi E., Renzini A., Kong X., Cimatti A., Broadhurst T., Alexander D. M., 2010, ApJ, 715, 385

Ouchi M. et al., 2004, ApJ, 611, 660

Papovich C. et al., 2010, ApJ, 716, 1503

Pettini M., Pagel B. E. J., 2004, MNRAS, 348, L59

Pozzetti L., Mannucci F., 2000, MNRAS, 317, L17

Rosati P. et al., 2009, A&A, 508, 583

Schlegel D. J., Finkbeiner D. P., Davis M., 1998, ApJ, 500, 525

Skrutskie M. F. et al., 2006, AJ, 131, 1163

Stanford S. A., Eisenhardt P. R., Dickinson M., 1998, ApJ, 492, 461

Stanford S. A. et al., 2006, ApJL, 646, L13

Steidel C. C., Adelberger K. L., Dickinson M., Giavalisco M., Pettini M., Kellogg M., 1998, ApJ, 492, 428

Suzuki R. et al., 2008, PASJ, 60, 1347

Tadaki K., Kodama T., Koyama Y., Hayashi M., Tanaka I., Tokoku C., 2011, PASJ, 63, S437, arXiv:1012.4860

Tanaka M., Finoguenov A., Ueda Y., 2010, ApJL, 716, L152

Tanaka M., Kodama T., Arimoto N., Okamura S., Umetsu K., Shimasaku K., Tanaka I., Yamada T., 2005, MNRAS, 362, 268

Tanaka M., Lidman C., Bower R. G., Demarco R., Finoguenov A., Kodama T., Nakata F., Rosati P., 2009, A&A, 507, 671

Tran K. et al., 2010, ApJL, 719, L126

Tremonti C. A. et al., 2004, ApJ, 613, 898

Ueda Y., Akiyama M., Ohta K., Miyaji T., 2003, ApJ, 598, 886

van Dokkum P. G., Franx M., Kelson D. D., Illingworth G. D., Fisher D., Fabricant D., 1998, ApJ, 500, 714

Yagi M., Kashikawa N., Sekiguchi M., Doi M., Yasuda N., Shimasaku K., Okamura S., 2002, AJ, 123, 66

Yan R., Newman J. A., Faber S. M., Konidaris N., Koo D., Davis M., 2006, ApJ, 648, 281

Yoshikawa T. et al., 2010, ApJ, 718, 112

This paper has been typeset from a TEX/ LATEX file prepared by the author.